Journal of Molecular Liquids 414 (2024) 126148

Contents lists available at ScienceDirect

Journal of Molecular Liquids

journal homepage: www.elsevier.com/locate/molliq

A paradigm for natural eutectic solvents based on fatty acids: Molecular interactions and toxicological considerations

Sonia Martel-Martín [a], Maria Enrica Di Pietro [b], Alberto Gutiérrez [c], Nuria Aguilar [c], Alfredo Bol-Arreba [a,d], Santiago Aparicio [a,c,*], Fatima Matroodi [e,f], Barbara Rossi [e,g], Andrea Mele [b,**]

[a] International Research Centre in Critical Raw Materials-ICCRAM, University of Burgos, 09001 Burgos, Spain
[b] Department of Chemistry, Materials and Chemical Engineering "Giulio Natta", Politecnico di Milano, 20133 Milano, Italy
[c] Department of Chemistry, University of Burgos, 09001 Burgos, Spain
[d] Department of Physics, University of Burgos, 09001 Burgos, Spain
[e] Elettra Sincrotrone Trieste, S.S. 114 Km 163.5, Basovizza, 34149 Trieste, Italy
[f] Department of Physics, Shahid Chamran University of Ahvaz, Ahvaz, Iran
[g] Department of Physics, University of Trento, Via Sommarive 14, 38123 Povo (TN), Italy

ARTICLE INFO

Keywords:
Natural deep eutectic solvents
Fatty acids
Monoterpenoids
Modelling
UV Raman
NMR
Toxicity

ABSTRACT

In this work, we present experimental and molecular modeling results on archetypal hydrophobic natural deep eutectic solvents (NADES) based on fatty acids (octanoic and dodecanoic acid) and menthol, a representative monoterpenoid. Our goal is to provide a multiscale characterization to enhance the understanding of this field by studying these selected archetypical mixtures. We examine their liquid state properties, intermolecular forces, nanoscopic arrangements, toxicity, and environmental impact.

The computational study integrates quantum chemistry, molecular dynamics (both all-atom and coarse-grained approaches), and thermodynamic modeling (COSMO-RS approach) to analyze the fluids and their interactions with biological entities, such as proteins and plasma membranes. The experimental characterization focuses on elucidating intermolecular interactions and liquid phase dynamics using NMR spectroscopy, visible and UV Resonance Raman spectroscopy (UVRR). Notably, this is the first report of UVRR data on NADES.

Additionally, we simulate the effect of the molecular moieties forming the solvents on biological targets—-specifically, protein and cell membrane models –. This in silico analysis aims to rationalize and predict their potential toxicity.

Overall, our experimental findings and in silico simulations contribute to a deeper understanding of these novel solvents in terms of their network of interactions. Additionally, they highlight the potential impact on biological targets, providing new data to accurately define the eco-friendliness of type V DES and their suitability as sustainable alternatives to traditional molecular solvents.

1. Introduction

The quest for sustainable and environmentally friendly alternatives to conventional solvents has intensified over recent years [1]. Deep eutectic solvents (DES) have emerged as one such alternative, capturing the interest of researchers and industries alike [2]. DES are typically formed by the interaction of a hydrogen bond acceptor (HBA) and a hydrogen bond donor (HBD) at a specific molar ratio, resulting in a mixture with a melting point lower than the individual components and much lower than that predicted by assuming a thermodynamic ideal behaviour of the liquid phase [3]. According to the individual components, they may display several unique properties, such as low volatility [4], thermal stability [5], tunable polarity [6], biodegradability [7], and low toxicity [8], which combined with their suitable physicochemical properties [9], make them promising candidates for a wide range of applications in chemistry, materials science, and biochemistry [10,11].

* Corresponding author at: International Research Centre in Critical Raw Materials-ICCRAM, University of Burgos, 09001 Burgos, Spain.
** Corresponding author.
E-mail addresses: sapar@ubu.es (S. Aparicio), andrea.mele@polimi.it (A. Mele).

https://doi.org/10.1016/j.molliq.2024.126148
Received 6 June 2024; Received in revised form 17 September 2024; Accepted 26 September 2024
Available online 4 October 2024

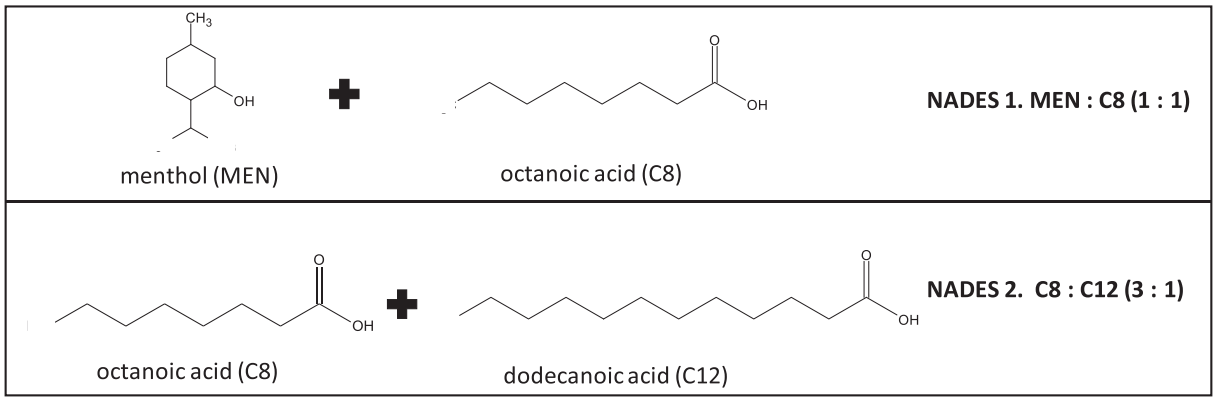

Fig. 1. Molecular structures of compounds used in this work and the developed NADESs.

Although some questions have been recently raised on the toxicity, sustainability and safety of large-scale use of DES [12–15], the possibility of avoiding these problems through a suitable selection of DES – components [16] among the plethora of molecules leading to DES, confirms the possibility of developing (‘*designer solvents*’) DES with properties tuned for specific technological applications [17].

Considering the different (HBA and HBD) components that upon mixing may lead to DES, they have been classified into five different categories [18], among which those labelled as Type V DES [19] are the most recent ones and have attracted great attention because of being formed by non-ionic components, which lead to even more suitable properties such as low viscosity [20]. Additional DES classification has been established considering their affinity towards water, having in mind that their possible hydrophilic nature has been a limitation for certain applications [21], e.g. catalysis or those requiring the solubilization of hydrophobic compounds [22], which has led to the search of hydrophobic DES (HDES) [23]. Likewise, HDES also show suitable physicochemical properties in comparison with hydrophilic ones, such as usually lower viscosity [24], especially when considering type V HDES. Noticeably, type V HDES not only emerged as a suitable platform for developing solvents for non-polar and hydrophobic substances, but indeed showed high versatility even in the field of metal ions extraction and separation form aqueous solutions [23,25,26]. Additional improvements on the development of DES considering environmental, toxicological and economical (low-cost) viewpoints may be reached when HBAs/HBDs of natural (vegetal) origin are applied, thus leading to the so-called Natural DES (NADES) [27]. Therefore, the group of type V hydrophobic NADES (V-HDES) may be considered as the most suitable DES group [28], considering economy, sustainability, toxicity and physicochemical properties, and thus, it was studied in this work using two archetypical fluids, Fig. 1: *i*) menthol (MEN) + octanoic acid (C8) in 1:1 mol ratio and *ii*) octanoic acid + dodecanoic acid (C12) in 3:1 mol ratio, although this last fluid is an ideal liquid mixture. It should be stressed, at this stage, that the choice of the model systems was largely dictated by the above-mentioned factors and the expected “fitness-for-use” as green, low melting mixtures to be used as solvents or extractants. This work has no aspirations to enter into the ongoing debate on the definition of DES and how profound the lowering of the melting point must be to earn the label “deep”. To avoid misunderstanding and over interpretation, from this point onward, the term V-HDES will be replaced by V-HES when referred to the model system here studied.

The consideration of fatty acids (C8 and C12) for the development of V-HES [29] was done owing to presence of large hydrophobic alkyl chains and carboxylic acid functional groups in their molecules, which have garnered considerable attention as potential HBDs for the design of hydrophobic DES [30] and resulting in promising hydrophobic DES with unique properties [31]. Likewise, fatty acids can be produced from waste oils through hydrolysis (using enzymatic or alkaline mechanisms) [32], and thus valorizing waste oils via V-HES production, which can be further applied for environmental remediation purposes, such as CO_2 capture [33] or water purification [30,34], extraction of bioactive compounds [35] or catalytic purposes [31], among other relevant applications.

The proper design and selection of suitable V-HES for the proposed applications requires a deep knowledge of their physicochemical properties as well as their relationship(s) with molecular level nanostructuring in liquid phases, with particular attention to intermolecular forces, for which molecular simulation studies provide a suitable platform. Previous studies have proved that modelling methods such as molecular dynamics simulations (MD) [36] or those based in quantum chemistr [37] have provided detailed characterization of V-HDES nanoscopic properties. Likewise, spectroscopic methods, such as Raman measurements [29], or Nuclear Magnetic Resonance (NMR) studies [30,38], are also useful for V-HDES characterization. Therefore, a combined computational and experimental study is reported in this work, providing V-HES characterization based on quantum chemistry and MD paired with UV Resonance Raman (UVRR) and NMR studies. It should be remarked that this is the first study reporting UVRR measurements on any type of DES, considering its use for intermolecular forces characterization.

Likewise, although V-HES based on fatty acids have been proposed even for therapeutic applications as drug delivery vehicles of poor water soluble Active Pharmaceutical Ingredients, [39] their possible toxic effect and their role on biological systems have been in silico studied in this work using two different approaches considering the interaction of the considered V-HDES with: *i*) model proteins and *ii*) model plasma cell lipid bilayers. These studies provide a nanoscopic mechanistic insight on the behavior of the considered V-HDES when in contact with biological targets.

In summary, this research paper aims to present a detailed investigation into hydrophobic natural deep eutectic solvents based on fatty acids. Through a combination of experimental data and molecular modeling, we aim to elucidate their unique properties, shed light on their diverse applications, and provide insights into their toxicity and environmental impact, proving their suitability for developing sustainable processes.

2. Materials and methods

2.1. Chemicals, V-HES preparation and accidental ester formation

The HBA and HBD compound used for V-HES were obtained from commercial sources with purities as reported in Table S1 (Supplementary Information). V-HES, Fig. 1, were prepared by the heating method as described elsewhere [40]: suitable amounts of the two components were weighted into a screw-capped sample vial using

an analytical balance (OHAUS Explorer, ±1 10^{-4} g), and mixed under stirring at 60 °C, using a thermoregulated bath (VFT Fuzzy Logic Thermoregulator, Fisherbrand), up to liquid phase formation.

The water content of the V-HDES samples measured by Karl Fisher titration with a Metrohm 870 KF Titrino Plus instrument previously calibrated was below 0.05 wt% ± 0.005.

The presence of hydroxyl and acid groups in the MEN and C8, respectively, may rise the doubt about the development of a possible esterification reaction, and thus to the simultaneous presence of DES and ester molecules in the prepared systems. Hümmer et al. [41] studied the reaction among MEN and fatty acids in neat DES and in presence of lipase as catalyst. Their results indicated that in absence of catalyst and for initial low water content, this water content remains almost constant after 24 h incubation, consistent with negligible esterification immediately after the mixing of the components. Similar results were reported by Martins et al. in the case of MEN – fatty acid DES [42]. However, in the present work the MEN – C8 esterification reaction was also considered as side and unwanted reaction. The detection and quantification methods for the ester formation were based on NMR and Raman spectroscopies and are briefly described in the next section.

2.2. Apparatus and experimental procedures

Off-Resonance Raman spectra were recorded by using an integrated micro-Raman setup (Horiba-JobinYvon, LabRam Aramis) with exciting radiation at 632.8 nm. All the spectra were collected at room temperature. The resolution was set at about 0.7 cm^{-1}/pixel. Noteworthy, the 1720–1750 cm^{-1} spectral region was also used to monitor the accidental presence of ester from the menthol octanoic acid condensation [43].

UV Resonance Raman (UVRR) spectra were collected by using the UVRR set-up available at the BL10.2-IUVS beamline of Elettra Sincrotrone Trieste (Italy) [44]. The excitation wavelengths at 213 was provided by a CryLas FQSS 213-Q3 Q-switched DPSS laser. The Raman signal of the samples was collected in back-scattered geometry, analyzed via a single-pass Czerny-Turner spectrometer (Trivista 557, Princeton Instruments, 750 mm of focal length) equipped with holographic gratings at 3600 and 1800 g/mm and detected using a CCD camera. We collected UVRR spectra with a resolution of 1.9 cm^{-1}/pixel. Cyclohexane (spectroscopic grade, Sigma Aldrich) was used for calibrating the spectrometer. The final radiation power on the samples was kept at about 300 μW. Continuous spinning of the sample cell during the measurements made it possible to prevent the photo-damage effect due to prolonged exposure of the sample to UV radiation.

High-resolution liquid-state NMR measurements were carried out with a Bruker NEO 500 console (11.74 T) equipped with a direct observe BBFO (broadband including fluorine) iProbe and a variable-temperature unit (^{1}H resonance frequency of 500.13 MHz). The samples were transferred to 5 mm NMR tubes, equipped with a capillary containing deuterated dimethylsulfoxide (DMSO-d_6) and tetramethylsilane (TMS), as lock signal and chemical shift reference, respectively. Both tubes were flame-sealed immediately after preparation and NMR spectra were acquired without sample spinning over a temperature range of 288 K to 328 K, in 10 K increments, with a minimum of 30 min allowed for thermal equilibration. The instrument was carefully tuned, shimmed, and the 90° pulses calibrated. 1D ^{1}H spectra were collected with 16 scans using 32,768 points, over a spectral width of 12 ppm, according to the sample. The unwanted formation of mentyl octcanoate was monitored by the integral ratio of the peak at 4.34 ppm (assignable to H1 of menthyl octanoate, ddd, $J_1 = J_2 = 10.7$ Hz and $J_3 = 4.3$ Hz,) and that at 3.06 ppm (H1 of free menthol, ddd $J_1 = J_2 = 10.7$ Hz and $J_3 = 4.3$ Hz). Such a ratio was not computable on the freshly prepared sample and raised to 2.4 % (mol/mol) only after one month.

Pulsed-Field-Gradient (PFG) ^{1}H NMR was applied to determine the self-diffusion coefficients (D_i) of the individual species. The self-diffusion coefficients were determined using the bipolar pulse longitudinal eddy current delay (BPP-LED) pulse sequence. All experiments were carried out with a total of 8 transients per increment using 16,384 points in the F_2 dimension, over a spectral width of 12 ppm, according to the sample. The relaxation delay was set to at least five times T_1, and 8 dummy scans were programmed prior to acquisition. The pulse gradients were incremented from 2 to 95 % of the maximum gradient strength in a linear ramp with 32 steps. For each experiment, the duration of the magnetic field pulse gradients (δ) and the diffusion times (Δ) were optimized to obtain 95 % signal attenuation for the slowest diffusion species at the last step experiment. For MEN:C8, δ values were in the 1.5–2.4 ms range, while Δ values were 0.1–0.2 s long. For C8:C12, δ values were in the 1.3–1.8 ms range, while Δ values were 0.1–0.2 s long. The raw spectra acquired were subjected to manual phasing and automatic baseline correction. Data were processed using an exponential filter in F_2 dimension (LB = 0.3 Hz). Integrals were employed in the Bruker T_1/T_2 module of TopSpin to fit the Stejskal–Tanner relation [45]:

$$I = I_0 exp\left[-(\gamma g \delta)^2 D\left(\Delta - \frac{\delta}{3}\right) \right] \quad (1)$$

where I is the signal intensity with the gradient applied, I_0 is the echo intensity without field gradient, γ is the gyromagnetic ratio of the observed nucleus, and g is the maximum magnetic field gradient strength.

All signals were fitted with a mono-exponential function.

The temperature dependence of the self-diffusion can be fitted with the exponential Arrhenius equation to obtain the activation energy for diffusive flow, that is the amount of energy required for the molecules in the fluid mixture to diffuse:

$$D(T) = D_0 exp\left(-\frac{E_a}{RT} \right) \quad (2)$$

where D_0 is a preexponential factor for the diffusive flow, E_a is the activation energy, R is the gas constant, and T is the absolute temperature.

Linear fits of the Arrhenius plots were performed with OriginPro 2018.

2.3. Molecular modelling

Molecular modelling studies were carried out for MEN:C8 and C8:C12 1:1 dimers as well as for C8:C12 3:1 clusters, for different molecular orientations. Geometrical optimization calculations were carried out at BP86/def2-TZVP plus Grimme's D3 [46] theoretical level using Turbomole software [47]. Binding energy, ΔE, for the different clusters was calculated as the difference between the energy of the corresponding cluster and the sum of the corresponding monomers, considering basis set superposition error (BSSE) corrected via counterpoise method [48]. Topological analysis of intermolecular interactions was carried out with the Quantum Theory of Atoms in Molecule (Bader's QTAIM theory) [49] with MultiWFN software [50]. The QTAIM analysis of intermolecular forces was carried out considering electron density (ρe), and Laplacian of the electron density ($\nabla^2\rho_e$) of Bond Critical Points (BCPs, type (3, −1) in QTAIM). Electron localization function (ELF) and Core-valence bifurcation index (CVB [51]) were also calculated for the corresponding hydrogen bonding intermolecular regions. Likewise, Non-Covalent Interaction analysis (NCI [52]) analyses were also developed for the optimized clusters.

The DFT optimized structures were considered for the calculations of COSMO files at BP86/def-TZVP theoretical level for COSMOtherm calculations using COSMOthermX software [53]. All COSMO calculations were carried out using BP_TZVP_24 parameterization. COSMO files were considered to predict the properties of the considered V-HDES. COSMO calculations were carried out considering cosmo files for isolated HBA and HBD molecules.

Classical MD simulations were carried out using MDynaMix v.5.2 [54] software using the force field parameterization reported in Table S2

(Supplementary Information) for systems and conditions reported in Table S3 (Supplementary Information). Force field parameters were obtained from SwissParam database (Merck Molecular Force Field) [55], except atomic charges which were inferred from ChelpG charges obtained from DFT simulations as reported for the considered model clusters. Initial cubic simulation boxes were built with Packmol program [56]. Additional simulations were carried to describe V-HDES behavior at vacuum interface by placing a 150 Å vacuum layer on top of the V-HDES liquid layer in the *z*-direction. All simulations were carried out using periodic boundary conditions in the three space directions applying a three steps consecutive procedure: *i)* 1 ns NVT simulations at the corresponding temperature, *ii)* 10 ns NPT equilibration step, at each selected pressure–temperature condition and *iii)* 100 ns NPT production simulations at each selected pressure–temperature condition. The Nose-Hoover method [57] was used for pressure and temperature control, with 30 and 1000 ps as the time constants for the thermostat and barostat, respectively. The Tuckerman-Berne double time step algorithm [58] (with long- and short-time steps of 1 and 0.1 fs) was applied for solving the equations of motion. The Ewald method [59] (1.5 nm for cut-off radius) was applied for handling coulombic interactions. Intermolecular interactions were described with the Lennard-Jones potential with 15 Å cut-off distance and Lorentz-Berthelot mixing rules for cross terms. The visualization, analysis and postprocessing of MD trajectories was carried out using VMD [60] and TRAVIS softwares [61].

The possible biological negative effects of the considered V-HDES were investigated using the concept of Adverse Outcome Pathways (AoPs), which delineate the sequence of events from the molecular to cellular to organ levels that lead to the toxic effects of a substance on a living organism [62]. The initiation of this complex cascade of processes is often associated with a Molecular Initiating Event (MiE), being the interaction of chemicals with plasma (cell) membranes [63]. In this study, we aimed to understand the mechanisms of interaction between the V-HDES and model cell membranes, specifically a dipalmitoyl-phosphatidylcholine (DPPC) lipid bilayer, and to assess the changes in membrane properties in the presence of V-HDES in aqueous solutions. To achieve this, Coarse Grained Molecular Dynamics (CG-MD) simulations were employed. The choice to use CG-MD simulations for studying the interactions between V-HDES and lipid bilayers, instead of All Atom simulations, was motivated by several factors. Notably, the size of the systems under consideration, which encompassed water, V-HDES, and the lipid bilayer, involved a large number of atoms. Furthermore, considering the time scale required to observe lipid bilayer changes, CG-MD was deemed a computationally efficient approach. The CG-MD simulations were conducted with a focus on V-HDES in aqueous solutions at various concentrations as presented in Table S4 (Supplementary Information). The representation of V-HDES, water, and DPPC molecules in the CG simulations (beading) is reported in Fig. S1 (Supplementary Information). The parameterization of the CG force field was carried out in accordance with the Martini3 CG forcefield [64], which has been demonstrated to be suitable for describing DES [65]. The CG-MD simulations were conducted using the MESOCITE/Materials Studio software and followed a three-stage procedure: *i*) Energy Minimization: The geometry was optimized using a conjugated gradient method for energy minimization; *ii*) NVT Simulations: Subsequently, 1 ns NVT simulations were performed at 318 K, utilizing the Velocity Scale method for temperature control; *iii*) NPT Simulations: Finally, 500 ns NPT simulations were conducted at 318 K using the Nose thermostat and 1 bar with the Berendsen barostat. Throughout all simulations, a coupling constant of 1.0 ps was employed for the thermostat and barostat, and a time step of 20 fs was used. Electrostatic interactions were treated with the Ewald method, while van der Waals interactions were subjected to a group (bead) based cutoff method with a 15.0 Å cutoff radius.

Further investigations into the potential adverse biological effects of the analyzed V-HDES were conducted in silico by assessing the interactions between the V-HDES molecules and specific target biomolecules (proteins). To accomplish this, a group of 100 human proteins were selected, Table S5 (Supplementary Information). Docking calculations were performed for V-HDES clusters as from DFT optimized arrangements, with the purpose of evaluating their binding interactions with the selected proteins. The protein structures were obtained from the Protein Data Bank, and prepared using Autodock Tools, ensuring that the docking regions encompassed the entirety of the respective biomolecules, employing a non-guided docking approach. The docking studies were carried out using Autodock Vina [66], and the resultant docked structures were ranked based on their corresponding affinities, as indicated by the scoring metrics.

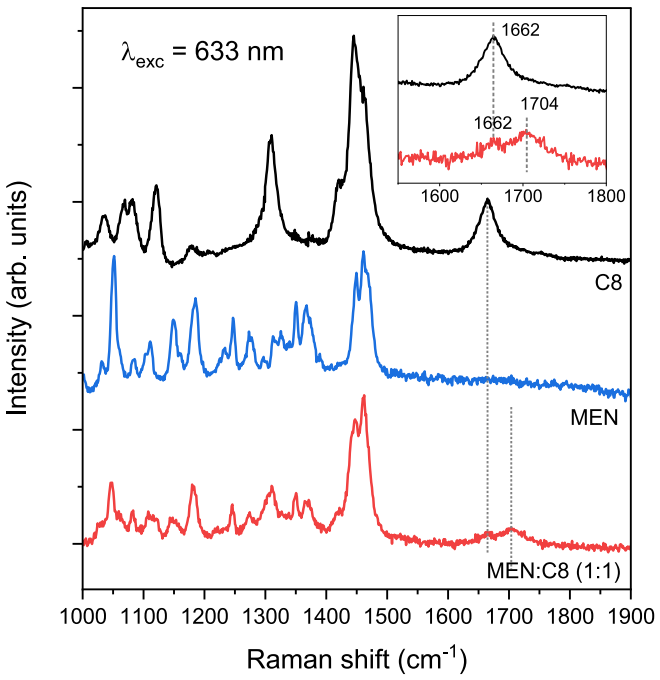

Fig. 2. Visible Raman spectra (excitation wavelength at 633 m) of MEN, C8 and MEN:C8 (1:1) in the spectral region between 1000 and 1900 cm^{-1}. From top to bottom: C8 (black trace), MEN (blue trace) and MEN:C8 (1:1) (red trace). The inset shows the spectral region of the C═O stretching vibrations. For clarity, the trace of MEN is not present in the inset, as no significant signals are in that region. The spectra in the inset have the same colour code as above.

3. Results and discussion

3.1. Visible and UV Resonance Raman studies

This section is focused on discussing the Raman spectra of MEN:C8 (1:1) V-HES collected using both an excitation wavelength far from resonance (λ = 633 nm) and an excitation wavelength in the deep UV range (λ = 213 nm). The fatty acids mixtures C8–C12 (3:1) actually exhibited extensive peak overlap of the individual components, thereby impeding the detection of selective band changes due to intermolecular interactions, and will not be discussed here.

Fig. 2 shows the comparison between the visible Raman spectra of the pure components MEN and C8 and the spectrum of MEN:C8 (1:1) collected at room temperature.

The spectrum of octanoic acid exhibits a peak attributable to C═O stretching vibration at about 1662 cm^{-1}, a band typically visible in the spectra of fatty acids in this spectral region [67]. In the corresponding range, the spectrum of MEN:C8 (1:1) V-HES shows two signals detected at about 1664 cm^{-1} and 1704 cm^{-1}, likely assigned to C═O stretching modes of C8. The signal at 1704 cm^{-1} does not fall in the region reported for the homologous modes of ester C═O, thus ruling out the formation of the menthyl octanoate (see Section 2). As a matter of fact, the MEN

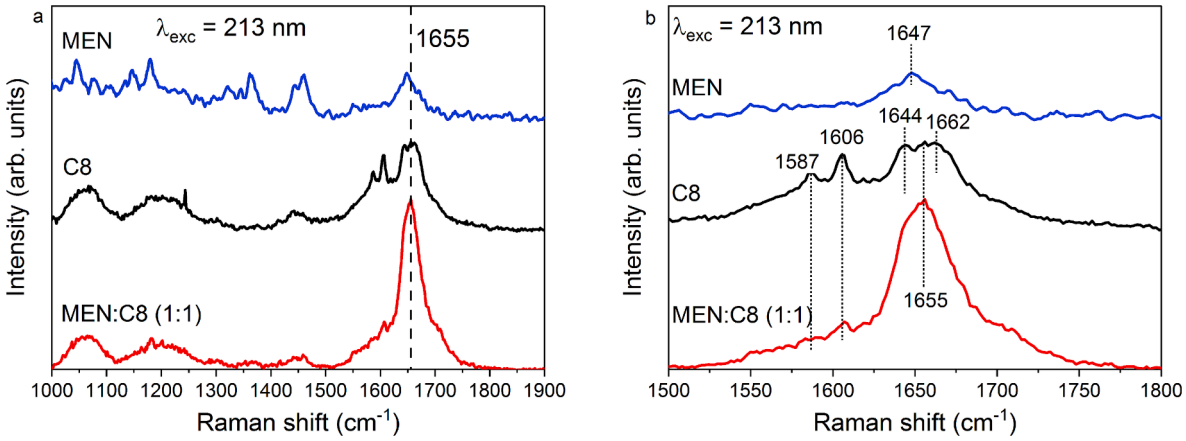

Fig. 3. A) UVRR spectra (excitation wavelength at 213 nm) of MEN, C8 and MEN:C8 (1:1) in the spectral region between 1000 and 1900 cm^{-1}. From top to bottom: MEN (blue trace), C8 (black trace), and MEN:C8 (1:1) (red trace). b) Expansion of the spectral region of the C═O vibration. The spectra have the same colour code as above.

Table 1
Molecular property changes upon hydrogen bonding formation for clusters reported in Fig. 6. *r* stands for the bond distances and *ν* for the stretching vibrational frequency corresponding to the reported bonds. The redshifted frequency is reported parenthesized.

	r (O— H)/ Å	*r* (C═O)/ Å	*ν* (O—H)/ cm^{-1}	*ν* (C═O)/ cm^{-1}
MEN (monomer)	0.975	–	3661	–
C8 (monomer)	0.982	1.223	3591	1693
C12 (monomer)	0.981	1.223	3591	1693
MEN at MEN:C8 1:1	0.981	–	2901 (−760)	–
C8 at MEN:C8 1:1	1.024	1.233	2792 (−799)	1642 (−51)
C8 at C8:C12 1:1	1.029	1.243	2740 (−851)	1630 (−60)
C12 at C8:C12 1:1	1.029	1.243	2740 (−851)	1630 (−60)

component does not give any spectral contribution above 1500 cm^{-1} (Fig. 2). The splitting of the C═O signal into two components suggests the presence of distinct C═O oscillators, i.e. ~1704 cm^{-1} (C═O weakly bonded) and ~1664 cm^{-1} (C═O strongly bonded) for C8 in the mixture with menthol. This finding can be interpreted as a local rearrangement at the main H-bond site, such as the carboxyl group, implying a potential alteration in H-bond arrangement from the pure acid to the menthol mixture. Despite the signal intensity being too low for a rational interpretation of peak shape, intensity, and wavenumber, a resemblance to the reported doublet for even fatty acids in the solid state due to dimer pair interactions [68] can be considered here.

As expected, the visible Raman spectrum of MEN:C8 shows, in the spectral region between 800 and 1500 cm^{-1}, many peaks attributable to both MEN and C8 although the spectrum of DES is not the simple linear combination of the spectra of the separate components. This confirms the establishment of some types of interactions between MEN and C8 in the eutectic mixture different from the H-bond. However, the strong overlapping of the bands in this spectral region makes the single decomposition of the Raman peaks of each component not reliable. For this reason, UV Resonance Raman experiments have been employed by choosing an excitation wavelength at 213 nm in close resonance with the electronic transitions of octanoic acid.

The UV Resonance Raman spectra collected with excitation wavelength at 213 nm exhibited a distinct pattern in the wavenumber region between 1200 and 1800 cm^{-1} as displayed in Fig. 3: a selective enhancement of octanoic acid Raman signals with respect to the menthol's band intensity, resulting in simplified spectra of MEN:C8 (1:1).

An illustrative example is presented in the right part of Fig. 3, showcasing the C═O stretching region (referenced to Fig. 2 for comparison). The UVRR spectrum of octanoic acid reveals a prominent band resulting from the contribution of at least three components observed at about 1662, 1655, and 1644 cm^{-1}. Additionally, two significant and previously unreported bands at 1606 and 1587 cm^{-1} are evident. The next section on DFT simulation provides several examples of the complexity of saturated fatty acids clustering via hydrogen bonding, thus providing a rationale for the C═O vibration wavenumbers distribution here observed and reported in the case of pure C8, where the same self-aggregation motives are likely to occur. Noteworthy, also the UVRR profile of MEN shows a previously unreported peak at 1647 cm^{-1}. Transitioning from the pure acid to the eutectic mixture, the signal at 1655 cm^{-1} becomes predominant in the spectrum and in reasonable agreement with the DFT calculated vibrational frequency (see Table 1) for gas-phase MEN:C8 (1:1) hetero-dimer. The strong increment of the intensity of the band at about 1655 cm^{-1} depicted in Fig. 3 reflects a substantial change in the local environment of the C═O oscillator associated with this signal, affirming the carboxyl group's pivotal role as the primary interaction site constituting the network in the bulk ES. Furthermore, the absence of a frequency shift is noteworthy, indicating that the strength of the H-bond network remains undisturbed upon mixing, despite alterations in local structuring. The DFT calculation section (vide ultra) provides a simple but realistic model spotting on the local changes of the C═O oscillators upon ES formation. A comparison of Fig. 6a and b points out the different H-bond motives in the 1:1 association of MEN and C8 on the one side, and the dimeric C8 on the other. Please note that, strictly speaking, Fig. 6b refers to the hetero-dimer C8–C12 but, considering the local environment of the carboxylic oscillators only, the C8–C12 hetero-dimer is a good approximation of the C8–C8 homo-dimeric association.

3.2. NMR studies

Representative ^{1}H NMR spectra acquired at 298 K on the two samples (MEN:C8 1:1 and C8:C12 3:1) are reported in Fig. S3. In both cases, a single peak for the exchangeable protons (—OH of MEN, here M10, and —COOH of C8 and C12, here A1) is observed, indicating a fast exchange in the NMR timescale.

The analysis of chemical shift variations gives preliminary hints into the strength of the intermolecular interactions experienced by the different species (Fig. 4). A marked low frequency (upfield) shift ($\Delta\delta = \delta(T) - \delta(288\ K) < 0$) is observed for exchangeable protons, indicating a weakening of H-bonds due to the increase in temperature [38,69–71]. At first sight, all other signals are barely affected, meaning they are not particularly sensitive to the temperature increase. If this is expected considering their weak or null involvement in the H-bond network, a

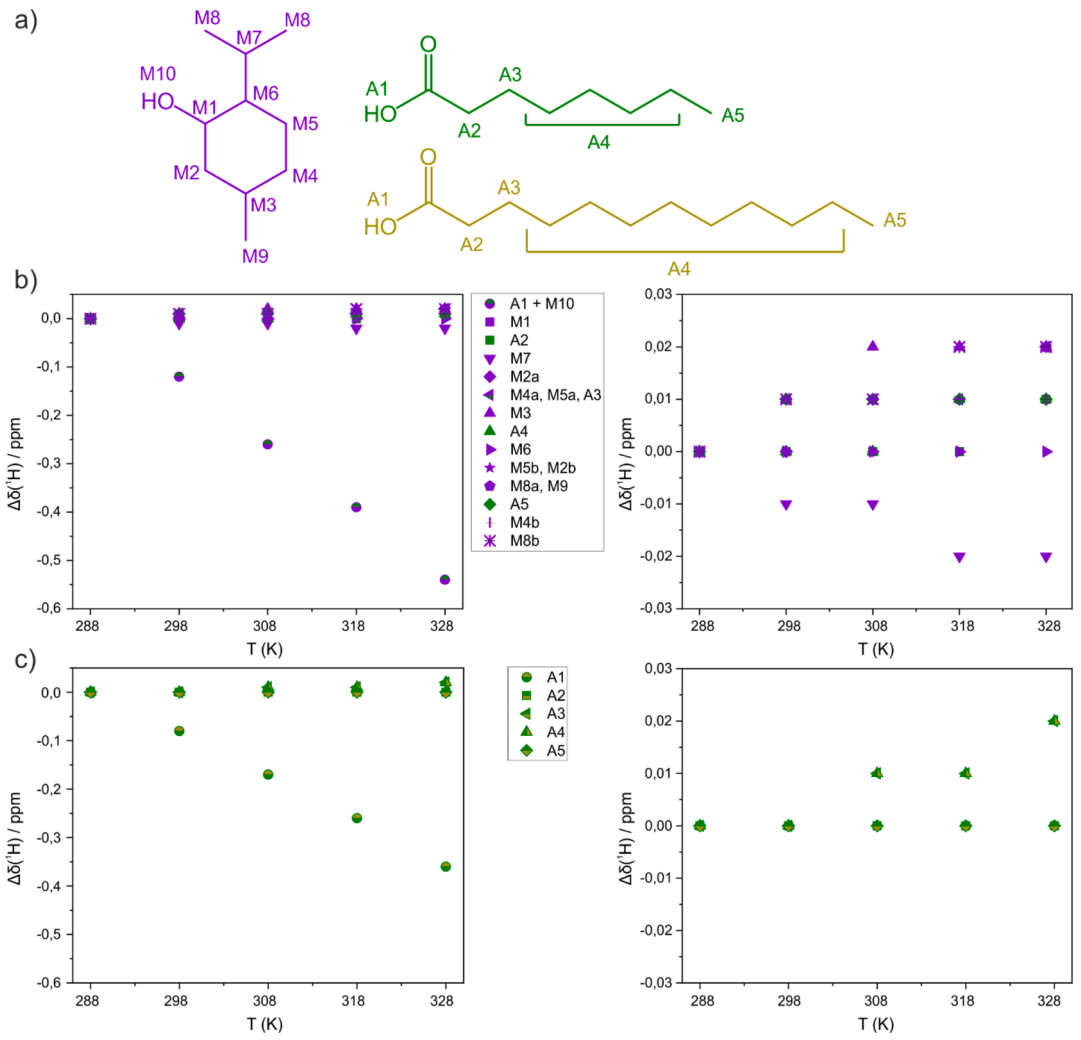

Fig. 4. Labelled structures of MEN, C8 and C12 (a). ^{1}H chemical shift variations of different proton sites in MEN:C8 1:1 (b) and C8:C12 3:1 (c) as a function of temperature. Δδ is defined as the chemical shift difference of each signal at a given temperature and at the lowest temperature (288 K).

closer inspection reveals a weak downfield shift ($\Delta\delta \approx 0.02\,ppm$) for protons M3, M4, M5, M8 and M9 in MEN:C8 and protons A3 and A4 in C8:C12 (see Fig. 4 for molecular sketches and atom labels). Despite a less intuitive interpretation, this would indicate that additional dispersive interactions do contribute to the intermolecular network of the eutectic and they are perturbed by the temperature increase [72]. Once again, as

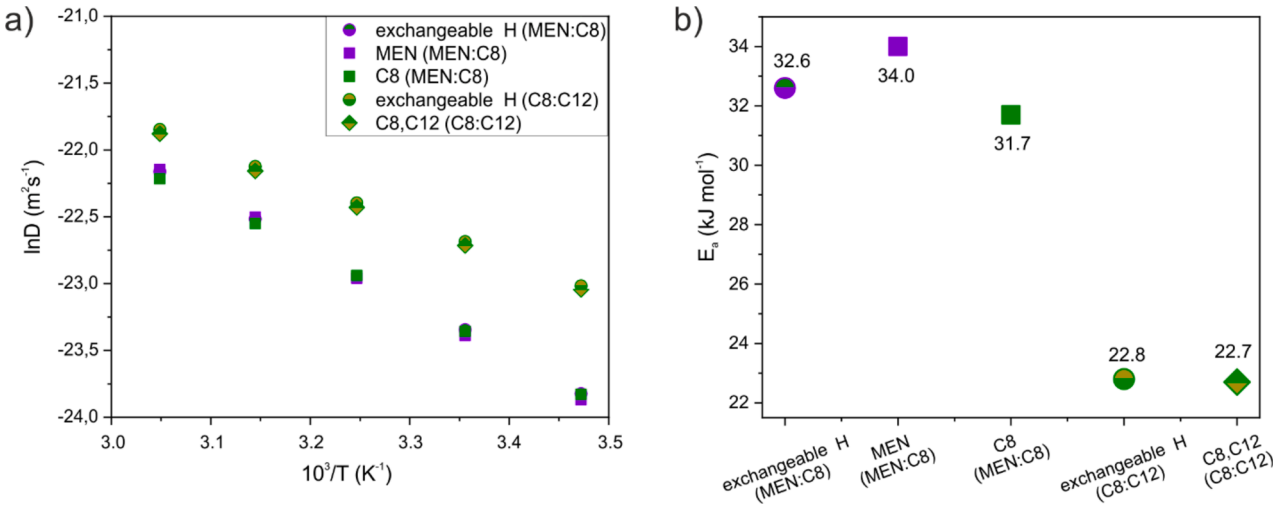

Fig. 5. Arrhenius plots showing the temperature dependency of the diffusion coefficients for the different species in MEN:C8 1:1 and C8:C12 3:1 (a) and apparent activation energies E_a (kJmol^{-1}) obtained from them. E_a are estimated to be accurate within ±5 %.

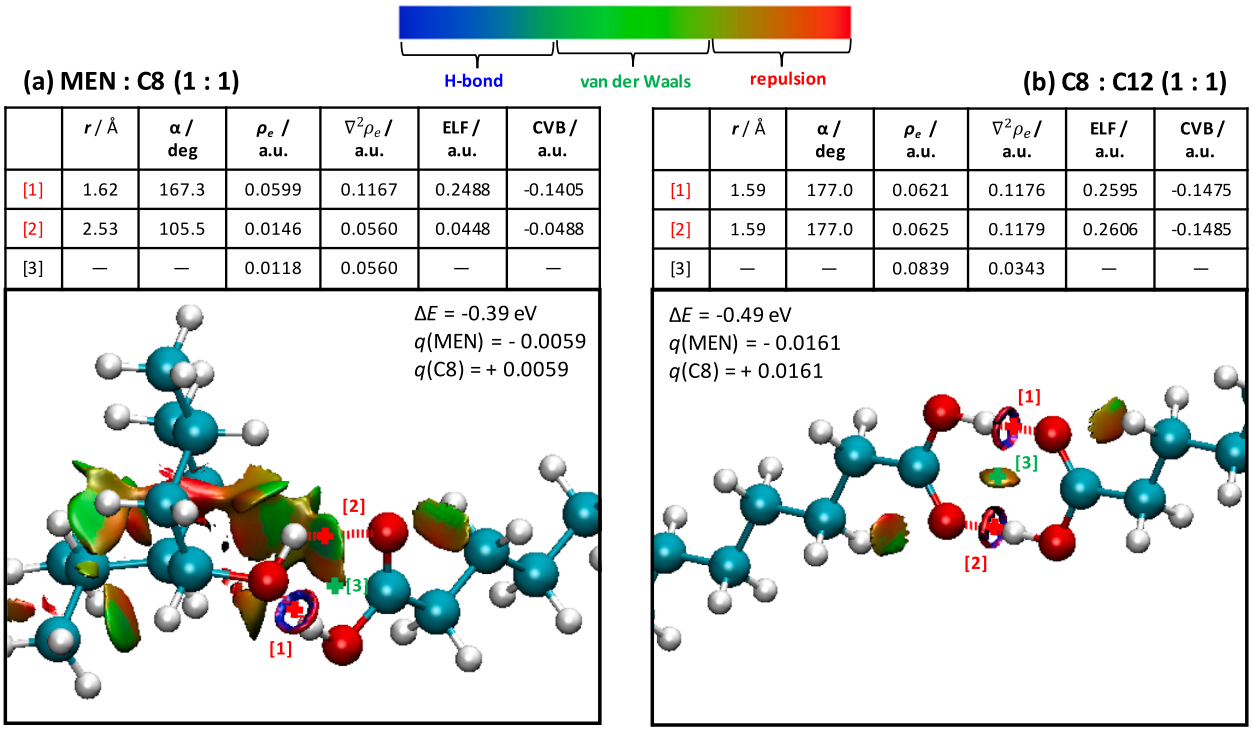

	r / Å	α / deg	ρ_e / a.u.	$\nabla^2\rho_e$ / a.u.	ELF / a.u.	CVB / a.u.
[1]	1.62	167.3	0.0599	0.1167	0.2488	-0.1405
[2]	2.53	105.5	0.0146	0.0560	0.0448	-0.0488
[3]	—	—	0.0118	0.0560	—	—

	r / Å	α / deg	ρ_e / a.u.	$\nabla^2\rho_e$ / a.u.	ELF / a.u.	CVB / a.u.
[1]	1.59	177.0	0.0621	0.1176	0.2595	-0.1475
[2]	1.59	177.0	0.0625	0.1179	0.2606	-0.1485
[3]	—	—	0.0839	0.0343	—	—

Fig. 6. Analysis of H-bonding in the considered NADES via the reported 1:1 dimers showing DFT optimized structures of MEN:C8 and C8:C12 1:1 clusters showing the lowest energy configurations including binding energy, Δ*E*, H to O distance (*r*), H-bond donor – acceptor angle (α, O–H — O), QTAIM properties (electronic density, ρ_e, and Laplacian of electron density, $\nabla^2\rho_e$), Electron Localization Function (ELF), Core Valence Bifurcation index (CVB), all these properties reported at the Bond Critical Point (BCP, red cross) and region corresponding to the reported hydrogen bonds (red dashed lines) as well as for the ring critical point (RCP, green cross). Total molecular charges (ChelpG) are also reported, *q*. NCI analysis is also reported showing the main types of intermolecular interactions. Only the molecular region around relevant hydrogen bonds is reported for both clusters.

previously underlined in the Raman spectroscopy section, the effect is weak compared to the one ascribed to H-bonding but not negligible.

PFG-NMR was applied to collect the self-diffusion coefficients of the different species in the mixtures (Table S6). Diffusion coefficients at room temperature are in line with those previously measured for the same systems [73] and higher than those previously reported for type III DES [67,69]. While in C8:C12 a single averaged self-diffusion coefficient is measured for the two molecular species, due to the structural similarities of the two acid components, in MEN:C8 (1:1) two diffusivities are observed for the terpene and the carboxylic acid. Noteworthy, MEN is slightly slower than C8 at lower temperature ($D_{MEN} = 4.3{\cdot}10^{-11}$ m^2/s vs $D_{C8} = 4.5{\cdot}10^{-11}$ m^2/s at 288 K), but gets faster at higher temperature ($D_{MEN} = 2.4{\cdot}10^{-10}$ m^2/s vs $D_{C8} = 2.3{\cdot}10^{-10}$ m^2/s at 328 K), with a crossover at intermediate temperature ($D_{MEN} = D_{C8} = 1.1{\cdot}10^{-10}$ m^2/s at 308 K). The temperature increase affects the mobility of MEN more than the carboxylic acids, likely due to the strongest involvement in the intermolecular network.

The apparent activation energies for the translational motion E_a were obtained fitting the diffusion data to an Arrhenius expression [74] and are reported in Fig. 5 and Table S7. E_a are in the order of 23 kJ/mol for the acid-based systems and approximately 10 kJ/mol higher for the MEN-containing system (32–34 kJ/mol), due to the stronger intermolecular network existing in the latter.

3.3. Molecular modelling: DFT

Intermolecular hydrogen bonding in the considered V-HDES were initially analyzed using DFT studies for model clusters starting from dimers (MEN:C8 and C8:C12 1:1 clusters, Fig. 6). The most stable dimers (i.e. largest Δ*E*) leads to the formation of complexes involving two hydrogen bonds per pair, i.e. cyclic structuring. In the case of MEN:C8, Fig. 6a MEN may act both as H-bond acceptor (hydrogen bonding [d1]) or donor (hydrogen bonding [d2]) with regard to C8, leading to large Δ*E* as a consequence of both interactions. Nevertheless, H-bond [d1] is remarkably shorter and stronger than [d2]. The QTAIM analysis is carried out considering that 0.002 a.u. $< \rho_e <$ 0.04 a.u. and 0.02 a.u. $< \nabla^2\rho_e <$ 0.139 a.u. ranges correspond to interactions that can be classified as shared based interactions or H-bond, with larger values indicating stronger interactions [75], with those values for interaction [d1] being on the top of the range, i.e. very strong H-bond, whereas those for [d2] indicate moderately strong H-bond. This agrees with ELF and CVB values, which in particular the largely negative CVB for [d1] indicates a very strong H-bonds. Therefore, although H-bond [d1] is remarkably stronger than [d2], both are present in the MEN:C8 interactions leading to a cyclic structure, as confirmed by the formation of a Ring Critical Point, Fig. 6a. The NCI analysis reported in Fig. 6a indicates a strongly interacting region around [d1] whereas a weaker one is obtained for [d2]. Additionally, the analysis of atomic charges shows almost negligible charge transfer between MEN and C8, thus the interaction between both molecules in developed via H-bonding. The results in Table 1 shows the changes in molecular properties both for MEN and C8 upon formation of cyclic H-bonding, the hydroxyl bonds both in MEN and C8 suffers elongation (specially C8) as well as the bond in C8 carbonyl group. This changes in bond properties are accompanied by changes in vibrational spectra as inferred from DFT, Table 1 [76].

For the C8:C12 interactions, an initial 1:1 cluster was built and optimized, Fig. 6b, showing a head-to-head association via two equivalent and strong H-bonds, as confirmed by the short donor – acceptor distance, the large values of QTAIM parameters, and ELF and large negative CVB. The NCI analysis shows two equivalent interaction regions corresponding to the developed H-bonds as well as another interacting regions around the developed RCP. Additionally, proper H-bonds are inferred as a result of the elongation of hydroxyl and carbonyl groups leading to large red-shifting of the corresponding stretching

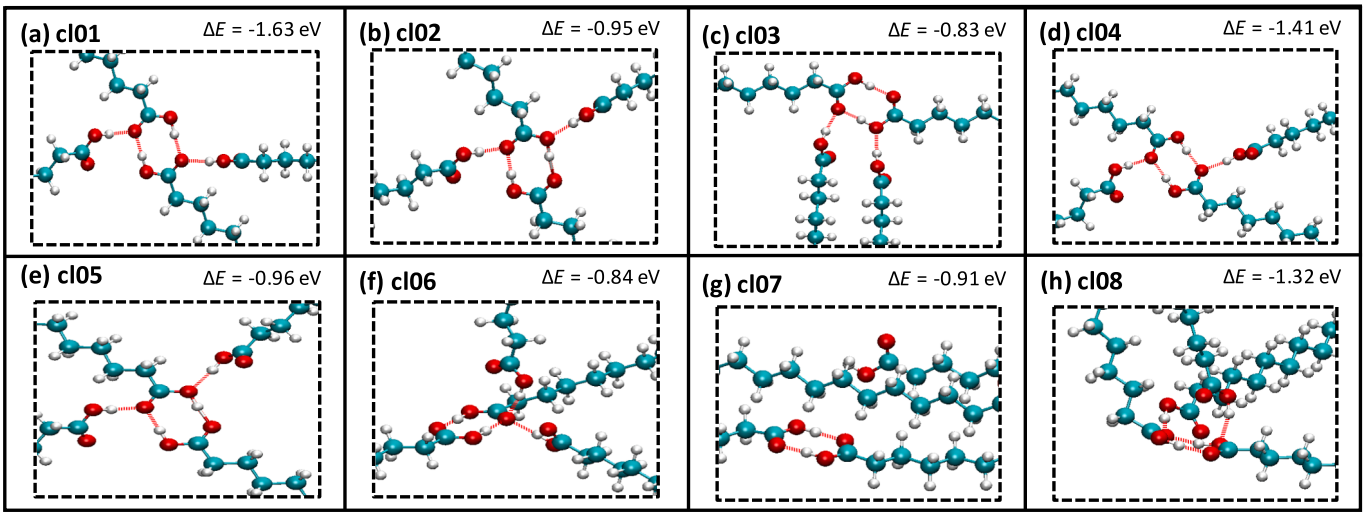

Fig. 7. DFT optimized structures of C8:C12 1:3 clusters for different molecular configurations including binding energy, Δ*E*.

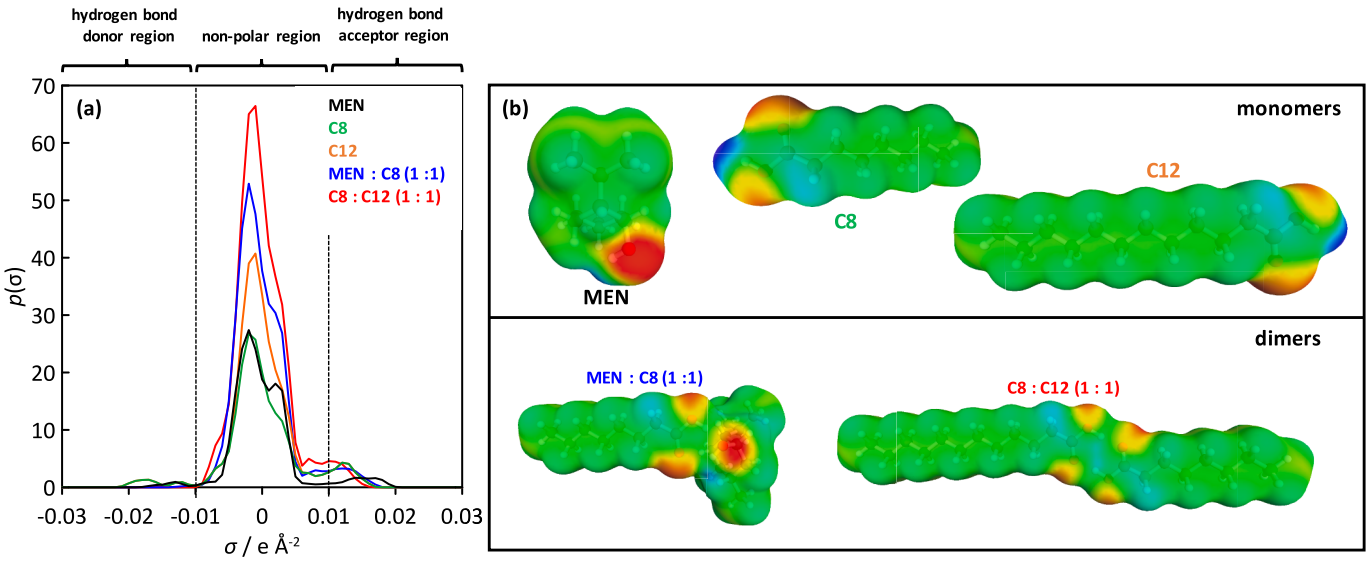

Fig. 8. COSMO sigma surfaces and profiles (polarization charge densities), σ, for the considered monomers and dimers.

frequencies, Table 1. As the V-HDES formed by C8 and C12 is considered for 3:1 mol ratio, although the 1:1 cluster model reported in Fig. 6b shows the formation of a largely stable structure via H-bonding, larger clusters are required to mimic the arrangements of C8:C12 3:1 V-HDES. For this purpose, different C8:C12 3:1 clusters were built considering different configurations, which were optimized, Fig. 7 (cl01 to cl08 clusters). All these clusters are based on the 1:1 cyclic structuring with additional neighbor C8 molecules placed around this central cyclic site. The reported cl01 to cl08 structures show very large Δ*E* (roughly two–three times the value for 1:1 cluster, Fig. 6b). In most of the cases, the C8 molecules develop additional hydrogen bonds around the cyclic dimer, leading to structures with four hydrogen bonds, thus large Δ*E*. Some clusters, e.g. cl01, cl04 and cl08, show remarkably large Δ*E*, which indicate further stabilization by the presence of surrounding C8 molecules. Additionally, cl07 shows that it is also possible that neighbor C8 molecules interact with the cyclic C8:C12 1:1 cluster via van der Waals interactions without developing H-bonding with the cyclic site leading also to large Δ*E*, as a consequence of the large number of available methyl/methylene groups, i.e. large number of carbon to carbon van der Waals contacts. The large Δ*E* for all the considered possible molecular arrangements reported in Fig. 7 indicate that all of them will be present in C8:C12 liquid phase at close to ambient temperatures, with the most remarkable feature being the formation of cyclic dimers and the remaining C8 molecules being placed in different arrangements, mainly H-bonded, around this site.

3.4. *Thermodynamic modelling: COSMO-RS*

The thermodynamic properties of the considered V-HDES were predicted using the COSMO-RS approach starting from *cosmo* files generated from optimized structures using DFT. The starting points for COSMO-RS calculations are the *cosmo* files, which upon visualization show charge accumulation or depletion visualized in the molecular surface and which through the so-called σ-profiles (Fig. 8) indicate the different molecular regions in terms of their ability for different types of hydrogen bonding. Results in Fig. 8a show the σ-profiles for isolated monomers as well as for the corresponding 1:1 clusters. MEN is characterized by a large non-polar region as well as by a hydrogen bonding acceptor and donor region around the hydroxyl group, Fig. 8b. In the case of isolated C8 and C12, the large non-polar region (alkyl chains) is

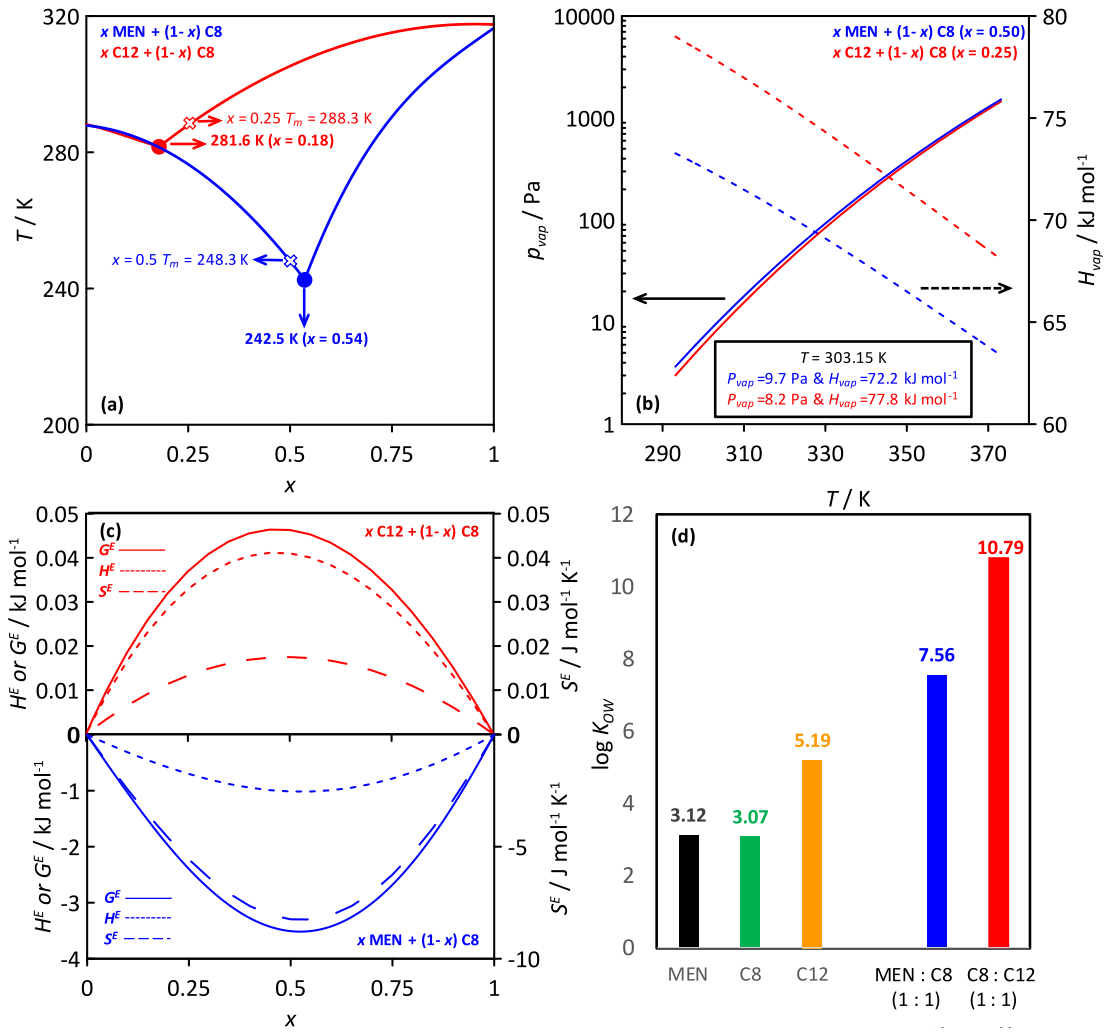

Fig. 9. Thermodynamics properties of the considered NADES. (a) Solid – liquid equilibria (indicating eutectic point as well as the compositions considered in this work), (b) vapor pressure, p_{vap}, (c) excess properties at 303.15 K (G^E, excess Gibbs free energy; H^E, excess enthalpy; S^E, excess entropy) and (d) octanol – water partition coefficient (K_{OW}).

accompanied by the acceptor and donor regions around the COOH groups, Fig. 8b. In the case of MEN:C8 1:1 cluster, upon formation of the dimer, the cluster is mostly the sum of the properties of the monomers, maintaining the donor and acceptor regions on the molecular surface, therefore being prone to develop further H-bonding through increase of the cluster size. For C8–C12, the large non-polar regions are accompanied by the exposed H-bonding acceptor sites, whereas the donor sites vanish, therefore the basic dimer structure is prone to act as acceptor for further H-bonds as showed in the model clusters reported in Fig. 7.

The main thermodynamic properties of the considered systems predicted via COSMO-RS are reported in Fig. 9. Solid-liquid equilibria as well as eutectic points are reported in Fig. 9a. For the case of MEN:C8, COSMO-RS predicts an eutectic composition almost at equimolar composition (x(MEN) = 0.54), which justifies the use of MEN:C8 1:1 considered in this work, with melting temperature much lower than ambient conditions, i.e. assuring liquid range for most of the possible applications. For the MEN:C8 1:1 (x(MEN) = 0.5), the COSMO-RS predicted melting temperature is 248 K, which is lower than the experimental value (262.8 K) reported in the literature [77], thus confirming the trend of COSMO modelling to underpredicts melting temperature for DES [78], although predictions can be considered reliable. In the case of C8:C12, COSMO-RS predicts an eutectic for C8-rich mixtures (x(C12) = 0.18), slightly different to the x(C12) = 0.25 used in this work. Nevertheless, the C8:C12 3:1 system is close to the predicted eutectic composition and the predicted melting temperature (288.3 K) justifies its use. Additionally, considering the non-ionic nature of the V-HDES, it is also relevant to analyze their possible vaporization as well as the properties of the vapor – liquid equilibria, Fig. 9b. The predicted vapor pressure at 303.15 K (slightly larger than ambient conditions) show very low volatile fluids for both cases, and although increasing vaporization upon heating is inferred, vapor pressures larger than 1000 Pa are only inferred upon heating to 373.15 K, i.e. not usual handling or using conditions. Likewise, both MEN:C8 1:1 and C8:C12 3:1 shows equivalent evaporation profiles. Therefore, combined results in Fig. 9a and b indicate that a suitable liquid range window can be considered for both fluids, assuring liquid phases and minor evaporation in a reasonable temperature range around ambient conditions. The low evaporation trends are justified by the large vaporization enthalpies reported in Fig. 9b (slightly lower for MEN:C8 than for C8:C12), which are produced by the strong hydrogen bonds inferred from results in Figs. 6 and 7.

The properties of the considered V-HDES, analyzed as a mixture of compounds, i.e. through the consideration of excess thermodynamic properties as a function of mixture concentrations, are reported in Fig. 9c. In this case, although for both systems property values shows maxima or minima around equimolar concentrations, which agree with the developed eutectic composition for MEN:C8 but not for C8:C12, the sign of the excess properties is different. In the case of MEN:C8, negative excess properties are inferred, the large (negative) excess Gibbs free

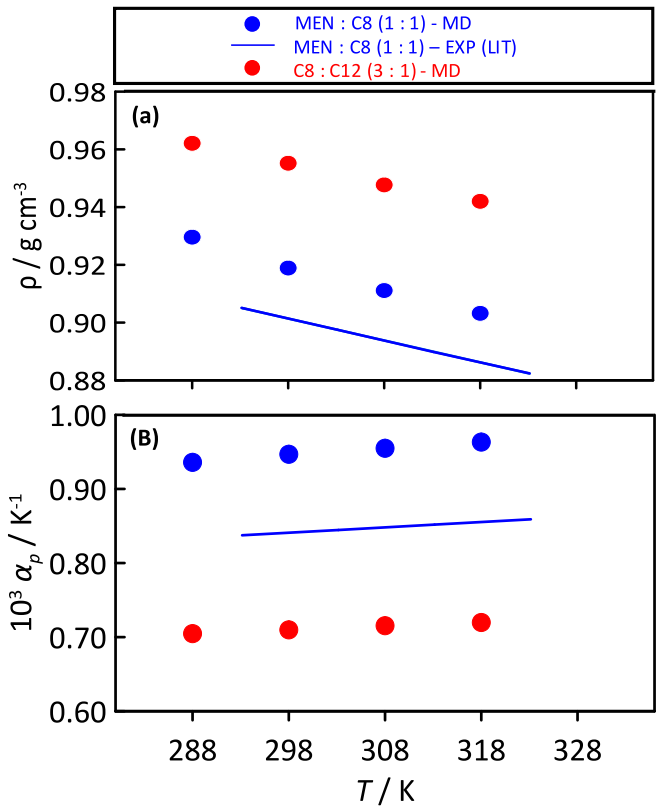

Fig. 10. Comparison between experimental (EXP(LIT)) [69] and MD simulations for density, ρ, and thermal expansion coefficient, α_p, as a function of temperature for the reported NADES-.

energy is produced by an exotermic mixing process accompanied by a remarkable negative excess entropy, both factors being justified by the different sizes and shapes of the mixed molecules (close to globular for MEN in contrast with linear for C8, Fig. 8b). The exothermic mixing process in MEN:C8 would arise from the strong hydrogen bonds between MEN and C8 molecules as reported in Fig. 6. In the case of C8:C12 although excess properties are positive they are almost negligible in comparison with those for MEN:C8, thus showing close to ideal mixtures, which is justified considering the equivalent trend to develop cyclic dimers both for C8 and C12 through homo- and hetero-associations. The slightly positive entropic effect, would be on the root of positive excess Gibbs free energy as a results of the disrupting effect in molecular packing upon mixing as a result of the different chain lengths and their effects on the development of asymmetric apolar domains.

The hydrophobic nature of the considered V-HDES is quantified through the predicted octanol – water partition coefficients, Fig. 9d. It should be remarked that isolated components show a largely hydrophobic character, especially C12, which is reinforced upon formation of the considered V-HDES. Results in Fig. 9d indicate that upon V-HDES formation, a synergistic effect is inferred regarding the hydrophobic character, which is beyond the mere sum of those of components, leading to largely hydrophobic fluids, thus indicting that these fluids can be used in different technologies without water cross-contamination, e. g. for water treatment operations and of pollutants, as well as considering that exposition to atmospheric humidity would not lead to relevant water sorption discarding the need of drying operations for the use of these V-HDES.

3.5. *Molecular modelling: MD*

The analysis of liquid phase nanoscopic properties was carried out using classical all atom MD simulations as a function of temperature for the two considered V-HDES. Initially, density and thermal expansion coefficient were predicted in the 288–318 K temperature range and compared with literature data for MEN:C8 1:1 [79], being in reasonable agreement with experimental data for both thermophysical properties, showing the reliability of the considered force field parameterization. C8:C12 is slightly denser than MEN:C8, although in both cases densities lower than water confirm their hydrophobic nature, Fig. 10a. Regarding thermal expansion coefficients, Fig. 10b, the reported values indicate that C8:C12 is more compressible than MEN:C8, because the long alkyl chain lengths in the considered fatty acids leads to less efficient molecular packings, i.e. larger free volumes forming more compressible

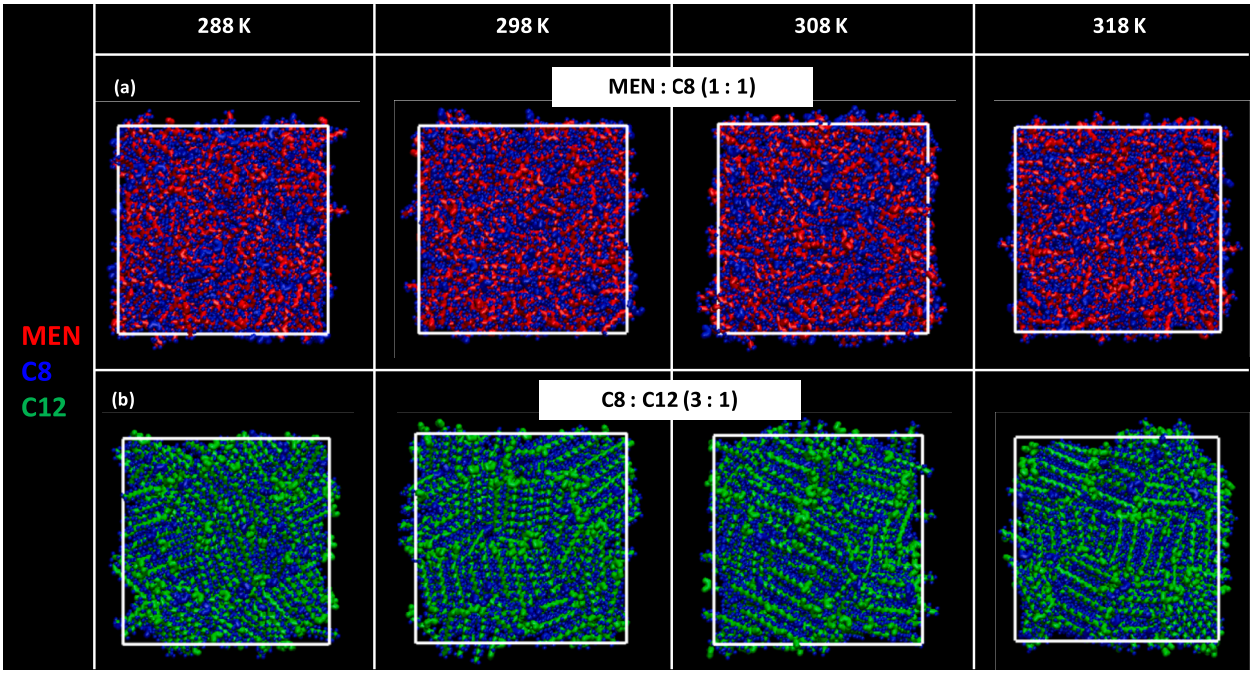

Fig. 11. Snapshots of nanoscopic liquid arrangements in the reported NADES from MD simulations at the reported temperatures.

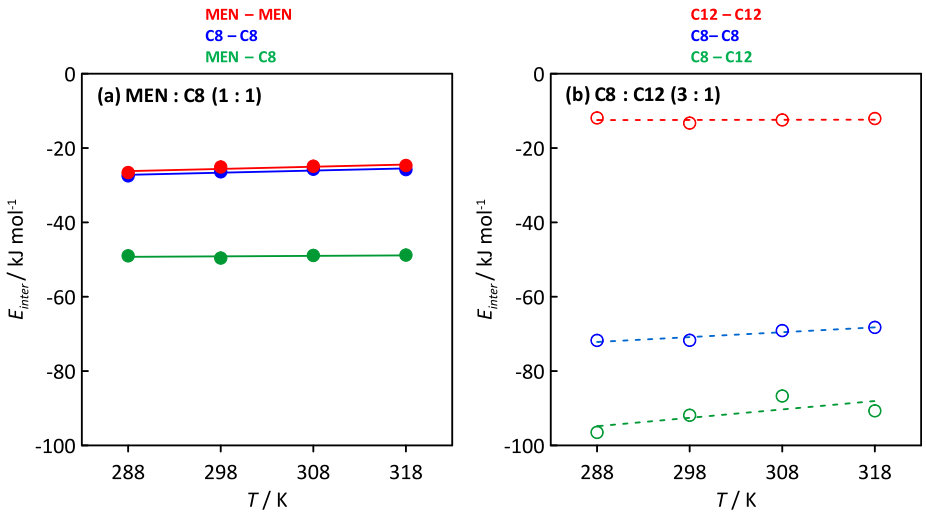

Fig. 12. Intermolecular interaction energy (Lennard-Jones contribution), E_{inter}, as a function of temperature for the reported NADES from MD simulations.

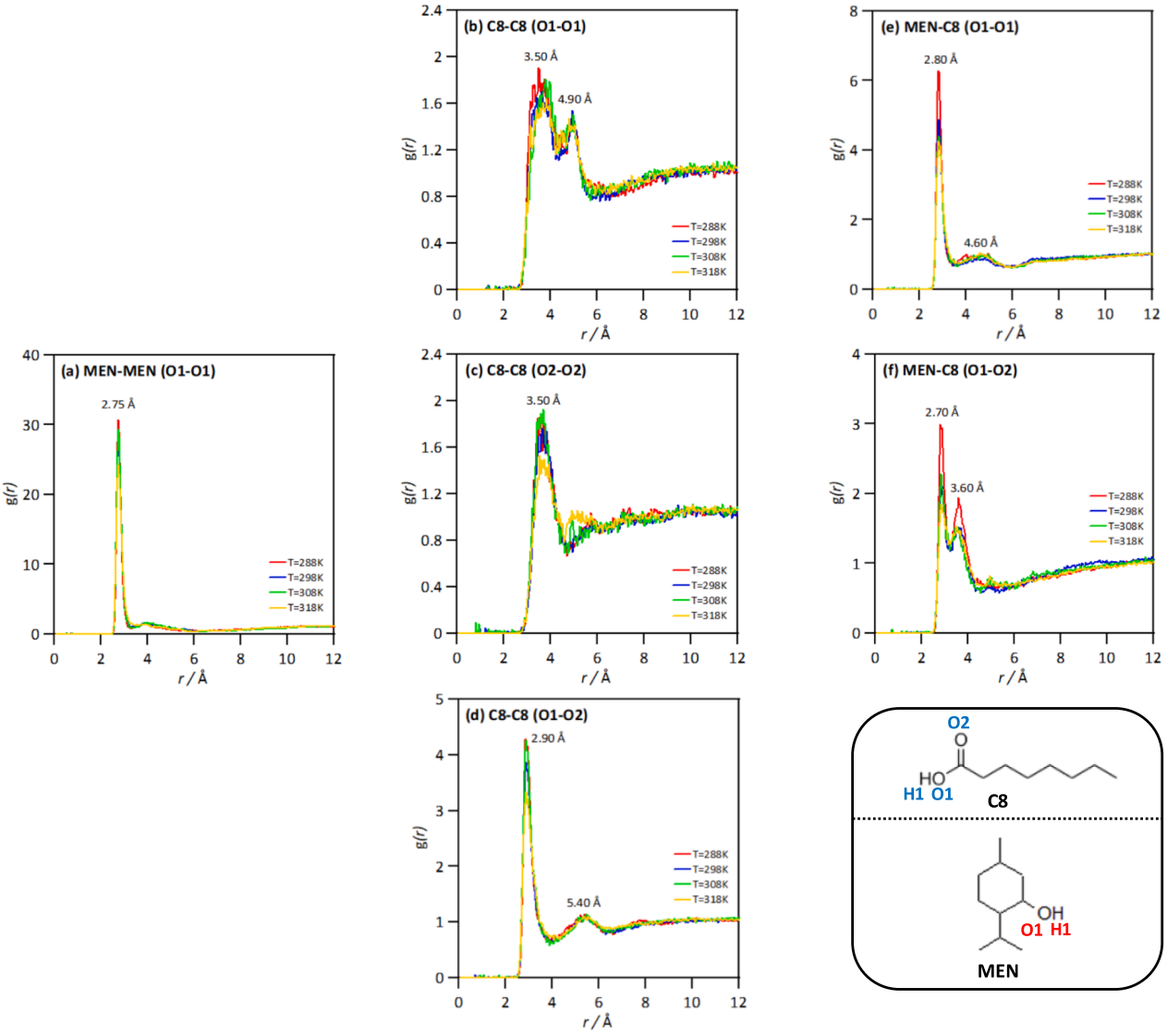

Fig. 13. Site – site Radial Distribution Functions as a function of temperature for the reported atomic sites in MEN:C8 (1:1) NADES as obtained from MD simulations.

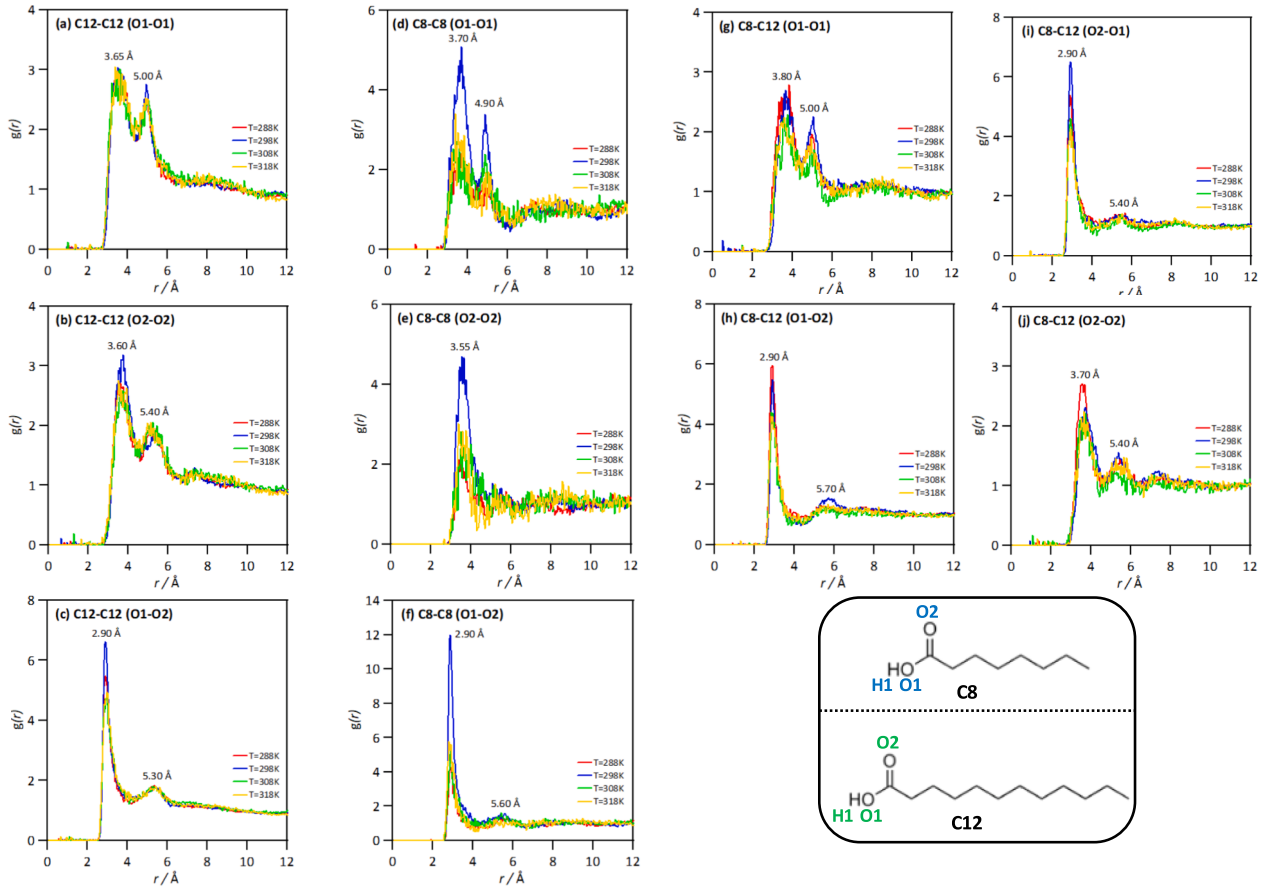

Fig. 14. Site – site Radial Distribution Functions as a function of temperature for the reported atomic sites in C8:C12 (3:1) NADES as obtained from MD simulations.

fluids (i.e. larger thermal expansion coefficients). Nevertheless, the thermal expansion coefficients are in the range of those for other V-HDES, e.g. 0.80 10^{-3} K^{-1} for the archetypical MEN: thymol [80], confirming that hydrophobic DES are more compressible (less dense) than hydrophilic ones [29].

The nanostructuring of the considered fluids is firstly analyzed considering the snapshots reported in Fig. 11 in the studied temperature range. Molecular arrangements are completely different for MEN:C8 than for C8:C12. In the case of MEN:C8, the presence of MEN molecules, with the strong tendency to develop MEN – C8 hydrogen bonds (Fig. 6), hinders C8 self-aggregation via alkyl chains stacking. In contrast, for the C8:C12 case, alkyl chains self-aggregation is clearly inferred, showing large domains with fully stacked apolar (pillar) domains, which is justified considering that this arrangement may be produced in parallel with the formation of hydrogen bonding dimers leading to exposed long alkyl chains, which may lead to a system stabilization via van der Waals contacts, Fig. 7. These arrangements are maintained with negligible disruptions in the studied temperature range and they will justify the low vaporization (Fig. 9b) of the considered fluids.

The strength of the interactions is quantified via the intermolecular interaction energy, E_{inter}, reported in Fig. 12. For MEN:C8, results indicate that homo (MEN – MEN and C8 – C8) and hetero (MEN – C8) interactions are present, although results indicate that hetero-associations prevail over homo-associations these are also present in the studied fluid. In the case of C8:C12, the role of van der Waals – like interactions is stressed as E_{inter} is four times larger for C8 – C8 than for C12 – C12, corresponding the larger C8 content in the studied V-HDES, and the C8 – C12 is also largely extended in the fluid. This confirms the mechanism of interaction reported in Fig. 11b for C8:C12 with chain stacking among all the available alkyl chains.

Intermolecular forces are analyzed via Radial Distribution Functions (RDFs) among relevant atomic sites, i.e. those involving hydrogen bonding, Figs. 13 and 14. In the case of MEN:C8, results in Fig. 13a confirms MEN – MEN self-aggregation via H-bonding as inferred from the narrow and intense RDF peak at 2.75 Å, which remains in the considered temperature range. Regarding C8 – C8 self-association, results in Fig. 13b to d, indicate preferential interaction via OH −C(O) sites, as confirmed by stronger and narrower peak in Fig. 13d in comparison with those in Fig. 13b, which show the formation of cyclic dimers because of the CO-CO peak reported in Fig. 13c. For the MEN – C8 hetero-association, the strong RDF peaks inferred both for MEN(OH) – C8(OH) and MEN (OH) – C8(CO), in this case with the development of a second intense RDF peak, confirms the formation of MEN – C8 cyclic dimers. These results confirm the mechanism of interaction obtained from DFT (Fig. 6) and observed with Raman spectroscopy and with NMR spectroscopy at increasing temperature (Fig. 3).

For the case of C8 – C12 a plethora of possible interactions are analyzed in Fig. 14. Results for fatty acid self-association, Fig. 14a–c for C12 – C12 and Fig. 14d–f for C8 – C8, show analogous patterns to those for C8 – C8 in MEN:C8 (Fig. 14b–d), and confirms that cyclic dimers by self-aggregation of each type of fatty acid are formed. Regarding C8 – C12 RDFs, Fig. 14g–j, results are analogous to those of C8 – C8 and C12 – C12, confirming that C8 – C12 H-bonds are developed through cyclic dimers but showing analogous properties top those also present formed by C8 – C8 and C12 – C12 self-associations. This behavior justifies the close to ideal behavior of C8 – C12 mixtures reported in Fig. 9c.

The integration of RDFs leading to the so-called solvation numbers, i.e. the number of atoms around a central one at a fixed distance, is reported in Fig. S2 (Supplementary Information) for the first RDF peak (i.e. first solvation shell), both for MEN:C8 and C8:C12. In the case of MEN:C8, Fig. S2a (Supplementary Information) results indicate large trend to MEN – MEN self-association but also MEN molecules H-bonded to C8 as

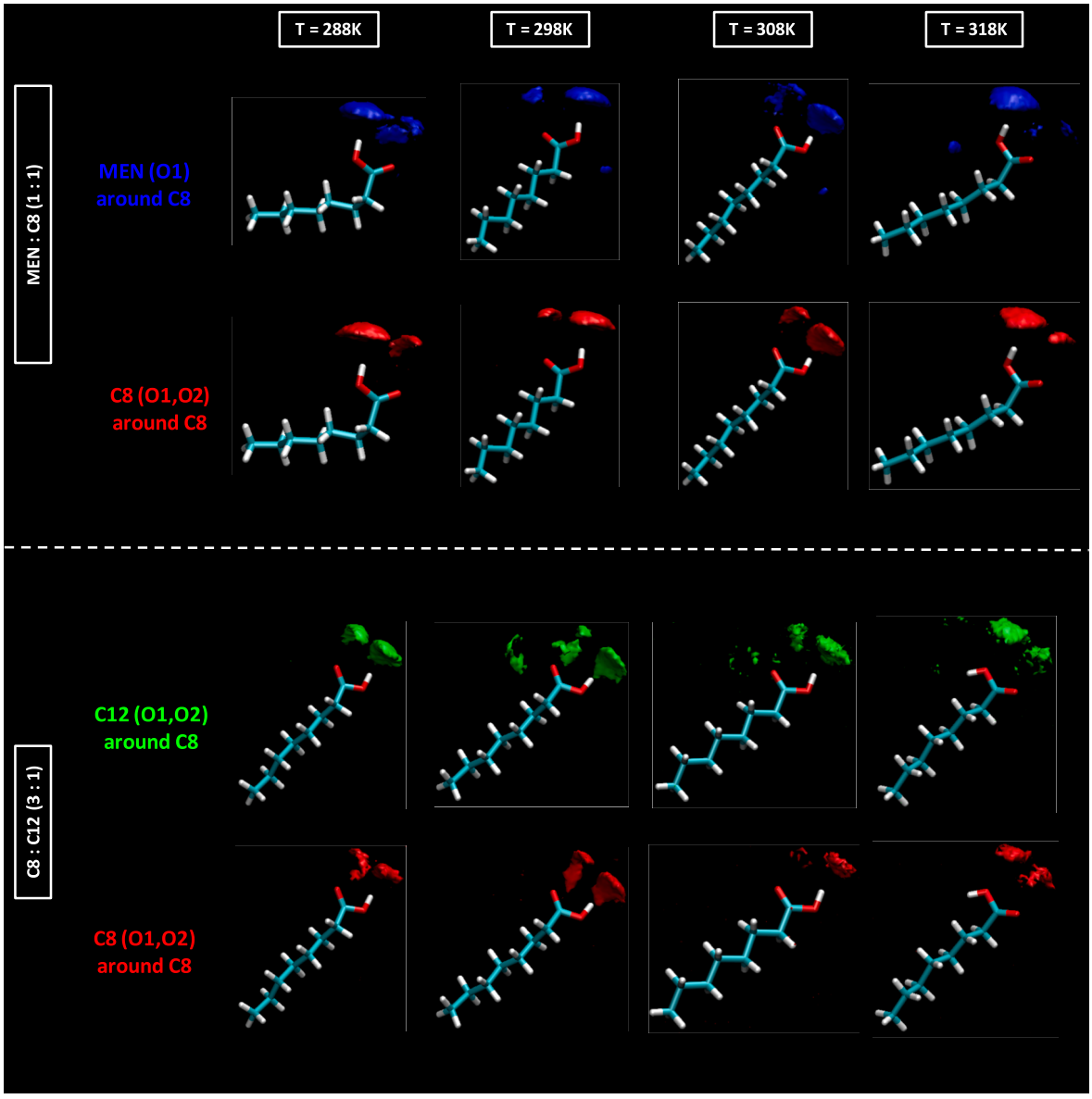

Fig. 15. Spatial Distribution Functions around C8 molecule as a function of temperature for the reported atomic sites in the considered NADES as obtained from MD simulations. Atom labels as in Figs. 13 and 14.

well as parallel C8 – C8 interactions. The experimental counterparts of these findings can be found in i) Raman spectra in non-resonant conditions, where the fingerprint profile of the MEN:C8 (1:1) mixture is far from the linear combination of the spectra of the individual components, and ii) NMR data obtained at different temperature (Fig. 4) showing a low but detectable sensitivity of MEN and C8 C–H protons to temperature effects, thus monitoring the behavior of the molecular frames not directly involved in H-bonds. For C8:C12, Fig. S2b (Supplementary Information), results indicate that C8 – C12 interactions are developed in an extension intermediate between C8 – C8 and C12 – C12, which thus confirms that the presence of each type of interaction is a matter of composition in the mixtures, with one type of fatty acid being replaced by the other one, with almost negligible changes in the properties of H-bonds, thus leading to close to ideal systems. These arrangements remain unchanged upon heating in the considered temperature range.

Further details on nanoscopic arrangements are inferred from the Spatial Distribution Functions (SDFs) reported in Fig. 15 around central fatty acid molecules. For the MEN:C8 case, the distribution of molecules around a central C8 molecule shows that both MEN and C8 compete for H-bonding sites in C8, the two spots around the OH and CO groups in C8 confirm that both MEN and C8 develop hydrogen bonds via cyclic dimers with C8 molecules and MEN:C8 is characterized both by homo and heteroassociation of their components. In the case of C8:C12, analogous patterns are inferred for homo and heteroassociations between the involved fatty acids, thus again showing the dimerization via hydrogen bonding among COOH groups.

Although nature and formation of hydrogen bonds has been showed in the previous results, the extension of hydrogen bonding is quantified in Fig. 16 defining hydrogen bond via a geometrical criterion (3.5 Å and 150° for donor – acceptor separation and orientation). In the case of MEN:C8, a large competing effect of homo-associations (MEN – MEN and C8 – C8) is inferred leading to larger number than MEN – C8 interactions. Nevertheless, the three types of hydrogen bonds are present in the studied composition range. In the case of C8:C18, C8 – C12 heteroassociations are produced in similar extension to C12 – C12 and lower to C8 – C8, but the three types are also maintained upon heating. Therefore, the two considered V-HDES are characterized by homo- and heteroassociation via hydrogen bonding.

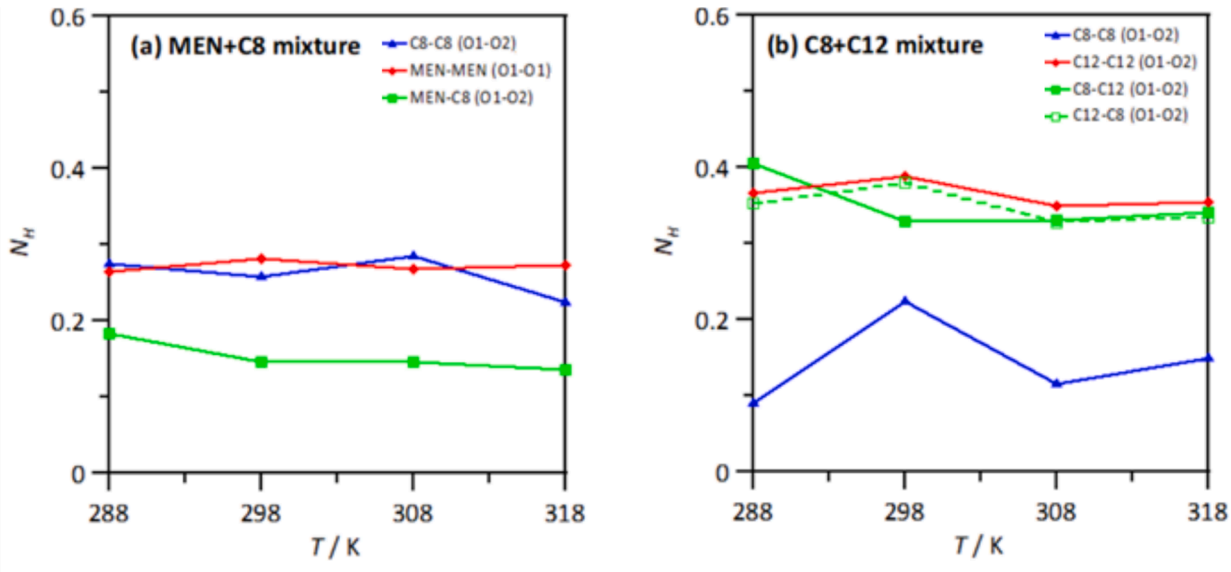

Fig. 16. Average number of hydrogen bonds per molecule, N_H, as a function of temperature for the reported atomic sites in the considered NADES as obtained from MD simulations. Atom labels as in Figs. 13 and 14.

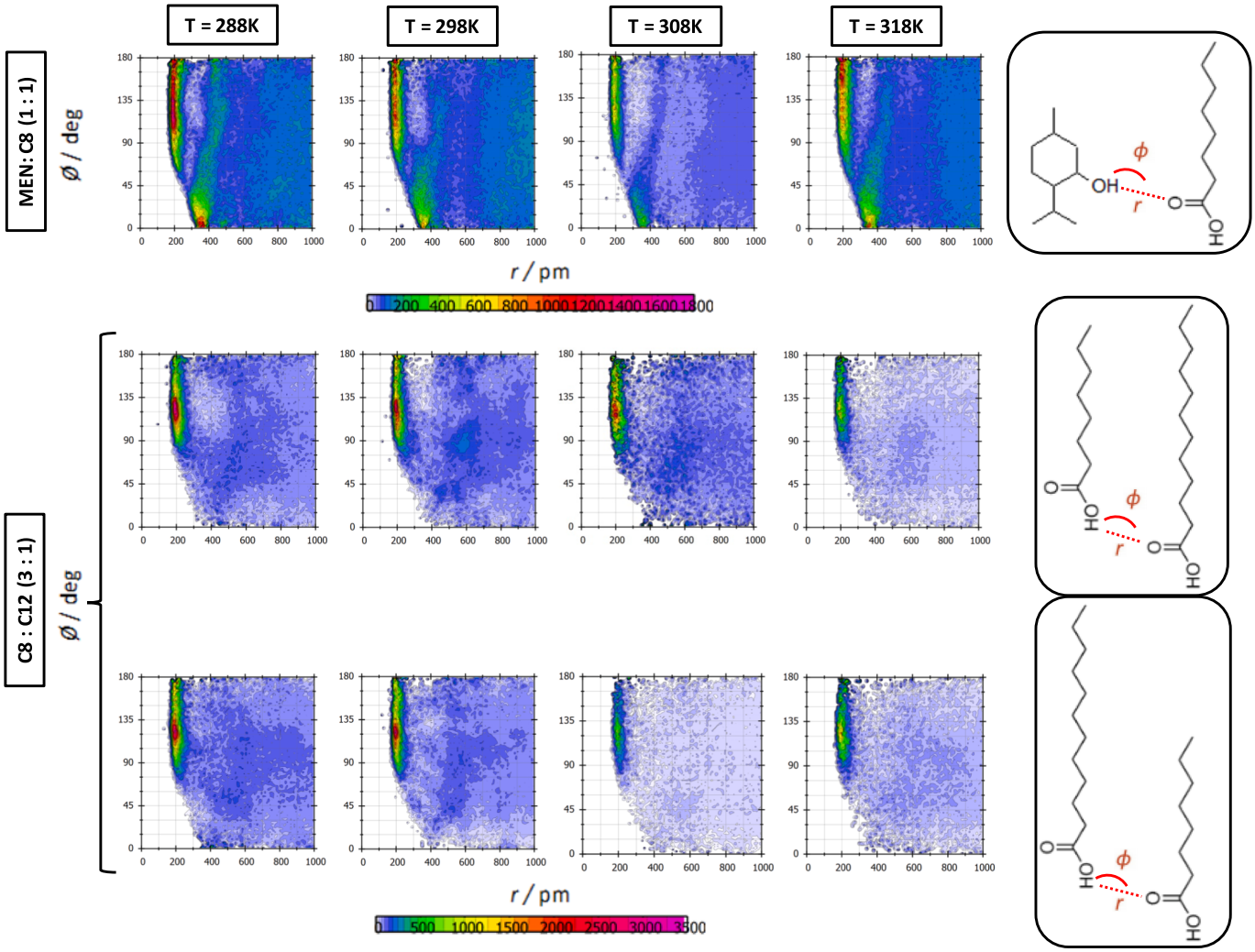

Fig. 17. Combined Distribution Functions for the reported intermolecular distances, r, and angles, φ, as a function of temperature for the reported atomic sites in the considered NADES as obtained from MD simulations.

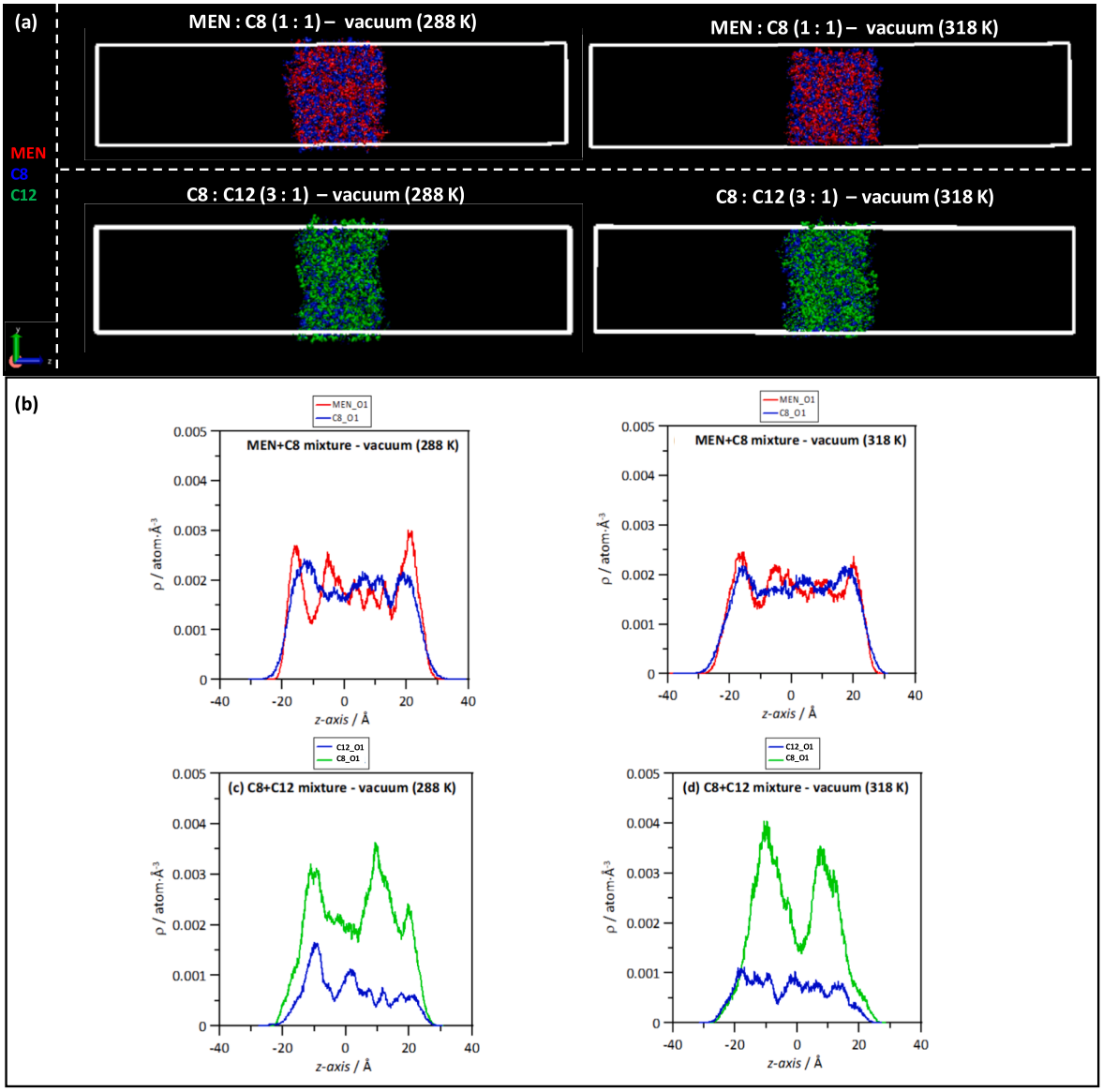

Fig. 18. Results for MD simulations of NADES – vacuum interfaces showing (a) snapshots of molecular distributions and (b) number density profiles in the direction perpendicular to the interface.

The geometrical characteristics of the developed hydrogen bonds are analyzed in Fig. 17 via the Combined Distribution Functions (CDFs) corresponding to the donor – acceptor separation and orientation. For MEN:C8, the MEN – C8 hetero-association is characterized by two spots corresponding to the two RDF peaks reported in Fig. 13f, showing a wide angular distribution, indicating flexibility by rotation of MEN molecule out-of-plane on top of the C8 but maintaining the H-bonds. In the case of C8 C12, the spots corresponding to the two hydrogen bonds in the cyclic dimer shows a narrow angular distribution, centered around 120°, which show a more rigid structure in comparison with MEN – C8. The weakening of the main CDF spots upon heating is the main effect inferred at higher temperatures indicating larger bending around the interacting sites but maintaining their main features.

The dynamics of the considered V-HDES was analyzed by calculating the self-diffusion coefficients, with those values obtained from MD simulations (Fig. S4, Supplementary Information) being in fair agreement showing those obtained from experiments (Fig. 5), thus probing how MD simulations are able to capture static and dynamic properties of the considered fluids.

To complete the analysis of the liquid properties of the considered V-HDES, the behavior at vacuum interface was also analyzed from MD simulations at two different temperatures (288 and 318 K), Fig. 18. The first main result confirms the almost negligible trend to evaporate of the considered fluids even under vacuum conditions, Fig. 18a, which agrees with the small vapor pressure reported in Fig. 9b. This absence of relevant evaporation stands on the strong hydrogen bonding for all the components of the systems via hydrogen bonding (homo and hetero-associations), which is maintained even upon heating. Regarding the molecular distribution at the interfaces, for MEN:C8 (Fig. 18b) there is an enrichment in MEN molecules at the interface, although this heterogeneity decreases upon heating. In the case of C8:C12, Fig. 18b, there is not any particular orientation at the interface and both molecules are present with larger content for C8 as a result of the larger number of C8 molecules in the C8:C12 3:1 system.

3.6. *In silico toxicological properties*

The possible toxic effect of the considered V-HDES was firstly analyzed via the interaction of DFT model clusters with a collection of human target proteins via molecular docking. (Table S5 Supplementary

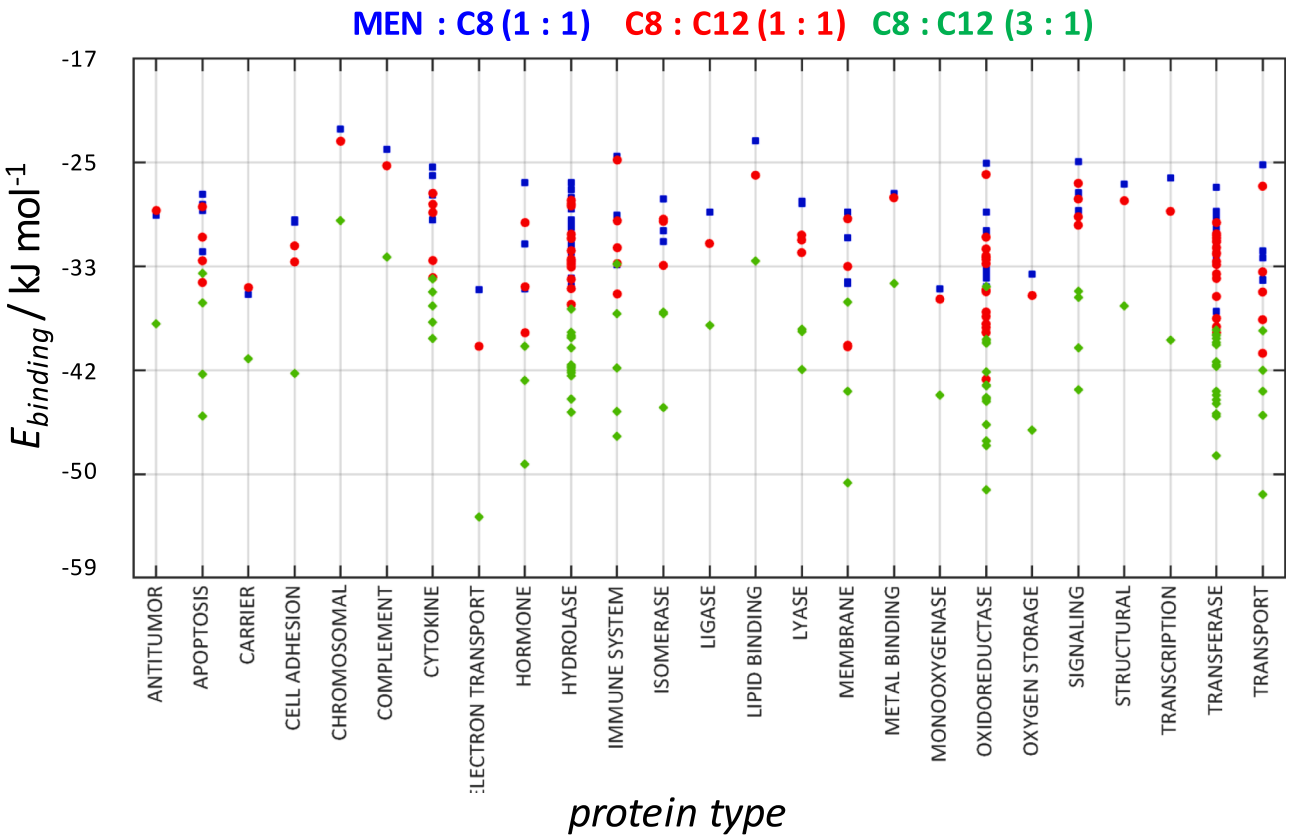

Fig. 19. Docking results for the reported molecular clusters (Figs. 6 and 7) reporting cluster – protein average binding energy ($E_{binding}$), as obtained from the 9-largest binding poses for each protein.

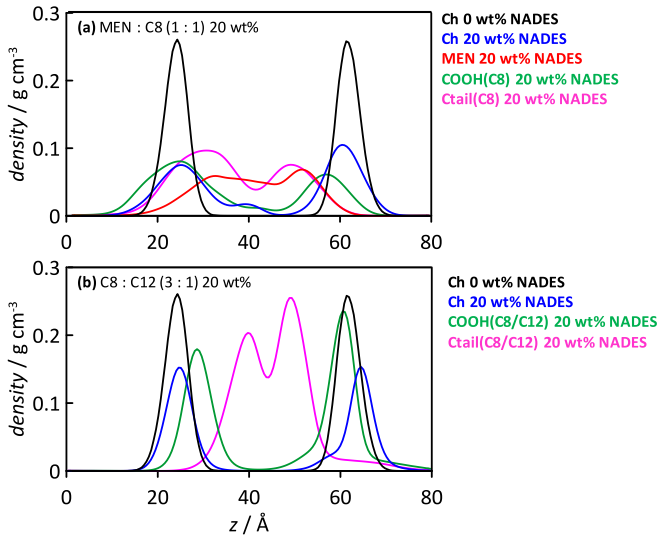

Fig. 20. Results of Coarse Grained MD simulations at 328 K and 1 bar for the interaction of the reported NADES in aqueous solution at 20 wt% in contact with a DPPC lipid bilayer. Results for neat water phase (0 wt%) are reported for comparison purposes. The distribution of choline bead and relevant NADES beads are reported in the direction perpendicular to the bilayer.

Information). It may be expected that, upon exposure to V-HDES, low concentrations may be present in organisms and thus model clusters may be representative of the molecular moieties reaching biomolecules such as proteins. The three model clusters (1:1 for MEN:C8 and C8:C12, as well as 3:1 for C8:C12) are considered for docking into proteins belonging to several groups having different biological functionalities.

Results reported in Fig. 19 show binding energies in the range – 22.6 to −27.7 kJ/mol, with remarkable larger values for C8:C12 3:1 clusters. The V-HDES – protein docking results indicate moderate to large affinity of the considered clusters for the studied proteins, being especially large for 3:1 clusters of fatty acids. The interaction of hydrophobic moieties with proteins has been previously reported for ionic liquids [81], concluding that large alkyl chains may interact with protein surfaces. Results in Fig. 19 confirm how increasing content of hydrophobic moieties in model clusters increase affinity toward all the considered proteins, and thus, strong binding may be inferred for large fatty acid content, i.e. leading to protein function disruption.

Further studies on possible biological effects of the considered V-HDES were carried out considering the interaction of V-HDES water solutions (20 wt%) with DPPC lipid bilayers as a model of the processes following V-HDES interaction with cell membranes. These studies, carried out using CG-MD simulations, show possible disrupting effects because of the V-HDES presence on the cell membranes functionalities. Results in Fig. 20 shows the distribution of V-HDES component in the region around the lipid bilayer. For MEN:C8 1:1, results of Fig. 20a show two main conclusions: *i*) the comparison with results in absence of the V-HDES show disruption of bilayer properties as inferred from the changes in the distribution of choline groups, *ii*) the V-HDES components penetrate into the bilayer, with MEN groups staying in the vicinity of inner glycerol DPPC groups, and C8 adopting a parallel distribution to the DPPC molecules with head COOH groups placed in the vicinity of head choline DPPC groups and alkyl chains placed along the inner apolar/hydrophobic region of the membrane. Therefore, large affinity for the DPPC molecules is inferred both for MEN and C8 components, thus leading to changes in the bilayer structuring. In the case of C8:C12, changes in the bilayer properties are also inferred, Fig. 20a, although lower disruption in the bilayer arrangement are produced as showed by the position of polar region (choline group) when compared with the

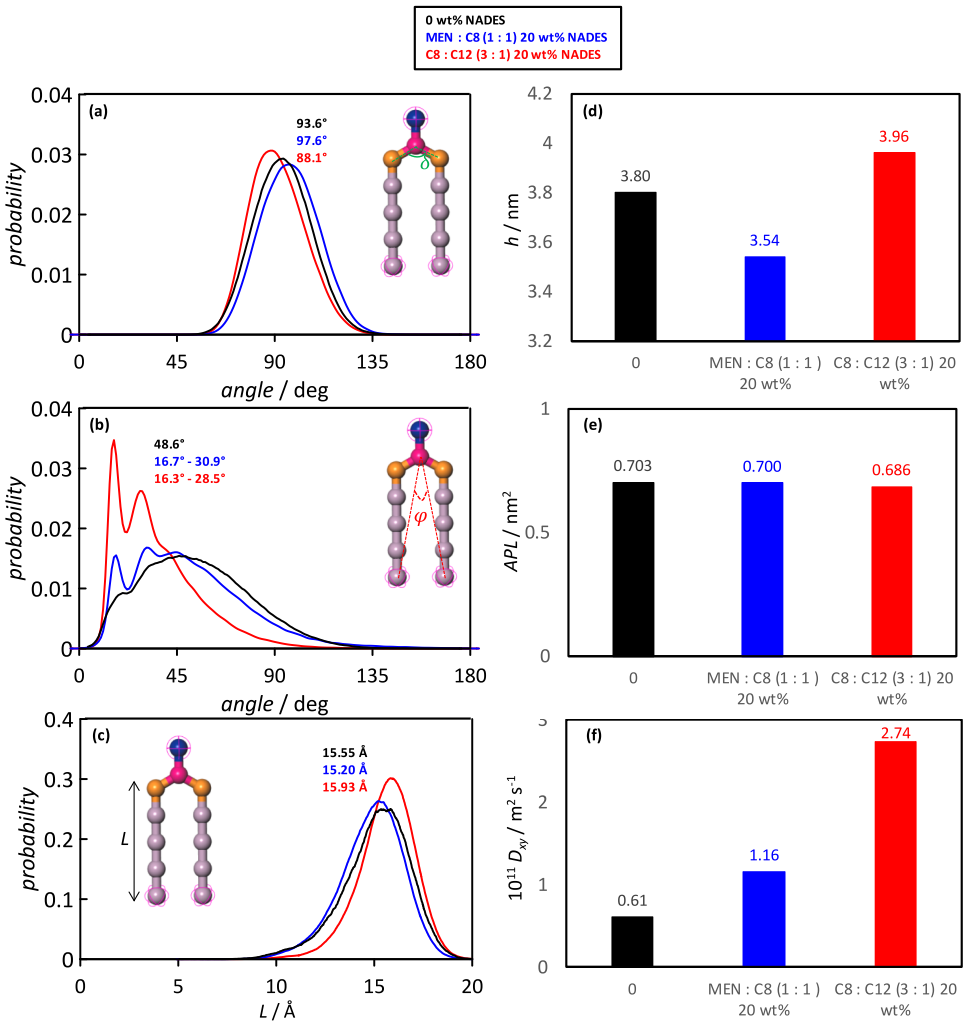

Fig. 21. Results of Coarse Grained MD simulations at 328 K and 1 bar for the interaction of the reported NADES in aqueous solution at 20 wt% in contact with a DPPC lipid bilayer. Results for neat water phase (0 wt%) are reported for comparison purposes. (a,b) Distribution of the reported angles in DPPC molecule; (c) distribution of the reported DPPC chain length; (d) lipid bilayer thickness, *h*, (e) area per lipid, *APL*; (f) DPPC lateral diffusion, D_{xy}.

case of MEN:C8 (the presence of polar and apolar moieties in MEN:C8 leads to disruption in different regions of the lipid bilayer). Both C8 and 12 are able to penetrate in the bilayer also adopting a parallel arrangement with DPPC molecules as for C8 in MEN:C8 V-HDES.

Changes in the lipid bilayer properties are quantified in Fig. 21. The DPPC relevant angles in the bilayer, internal polar angle (δ) and lipid head – tail (ϕ) suffer non-negligible changes in presence of both types of V-HDES, Fig. 21a and 21b, especially the ϕ angles, which are largely shifted toward lower values, indicating a compression of DPPC alkyl chains in presence of the fatty acids because of their insertion into the apolar bilayer region. Regarding the extension of lipid apolar chains, Fig. 21b, changes are also produced, especially for C8:C12 in which a chain length increase is inferred as a result of the decrease in ϕ angle. Regarding the bilayer width, Fig. 21d, MEN:C8 leads to a width decrease, whereas C8:C12 leads to a bilayer expansion. Therefore, the presence of MEN molecules in the V-HDES and their affinity for the polar head regions of the bilayers leads to disruption of the bilayer larger than for C8:C12, in which the fatty acids are inserted into the bilayer, increasing the bilayer length via apolar region increase in width, Fig. 21c. Results in Fig. 21e for Area per Lipid (APL), show minor changes in presence of the V-HDES, for C8:C12 the increase in ϕ leads to a slight compression of the bilayer, whereas for MEN:C8 the bilayer changes seem to be limited in the direction perpendicular to the bilayer (width, Fig. 21d), whereas in the APL no remarkable changes are produced. Finally, changes in the dynamic properties of the bilayer (fluidity) are quantified through the calculated self-diffusion coefficients in the bilayer direction (D_{xy}), Fig. 21f. The D_{xy} results show remarkable increase in the fluidity upon interaction with V-HDES, with larger effect for C8:C12. These results indicate that the presence of fatty acid and their arrangement into the lipid bilayer leads to a disruption of the bilayer caused by its position into the bilayer as inferred from Fig. 20. In the case of MEN:C8, although large structural disruptive effects are inferred from results in Fig. 21, specially in terms of bilayer width, the presence of MEN and its effective interaction with choline polar head groups decreases the effect of C8, which tend to increase fluidity, leading to a lower perturbation in terms of fluidity when compared with C8:C12. Therefore, the effects of the considered V-HDES on the lipid bilayer may be divided into *i*) structural (larger for MEN:C8) and *ii*) dynamic (larger for fatty acids). It may be concluded from the protein docking and lipid bilayer interaction studies, that the considered V-HDES leads to remarkable interaction with biological molecular entities.

4. Conclusions

The comprehensive analysis of the V-HDES based on the combination of different experimental and modeling approaches and in silico toxicological properties provides valuable insights into their structural, thermodynamic, and biological characteristics. The molecular modeling

employing DFT studies, sheds light on the formation of intermolecular hydrogen bonds within the V-HDES. The results show that the considered V-HDES exhibit strong hydrogen bonding interactions, leading to the formation of cyclic dimers in both MEN:C8 and C8:C12 systems. The extensive analysis of these interactions, as well as the changes in molecular properties and vibrational spectra, emphasizes the stability and structural characteristics of these systems. The combination of NMR and Raman data allowed to highlight selective molecular interactions, mainly but not exclusively based on H-bond. Considering that the examined systems are expected to show ideal mixing, particularly for C8:C12 systems, the data of this work demonstrate that a thorough structural investigation on the interacting systems is due also in the case of ideal mixtures.

The thermodynamic modeling using the COSMO-RS approach provides valuable insights into the thermodynamic properties of the V-HDES. The predictions of solid–liquid equilibria, eutectic points, vapor–liquid equilibria, and the hydrophobic nature of these fluids indicate their suitability for various applications, with a wide liquid range and minimal evaporation at ambient conditions. Molecular dynamics (MD) simulations reveal the nanoscopic properties of the V-HDES. The analysis of density, thermal expansion coefficients, and the distribution of components within the systems offers a detailed understanding of their behavior at different temperatures. These simulations show that the V-HDES maintain their stability, and their hydrophobic nature is highlighted. The in silico toxicological properties analysis suggests that V-HDES may interact with human target proteins and disrupt protein functionalities, especially in systems with a higher content of hydrophobic moieties. Additionally, interactions with lipid bilayers indicate that the V-HDES can perturb the structural and dynamic properties of cell membranes, with the degree of disruption depending on the specific V-HDES composition.

In summary, the results of this study highlight the potential utility of V-HDES in various applications due to their strong hydrogen bonding, favorable thermodynamic properties, and low evaporation rates. The interaction of V-HDES with biological molecules and cell membranes indicates a need for caution when considering their use in biomedical or biological contexts, as they may disrupt biological systems. It is important to note that the in silico toxicology findings serve as a starting point rather than a conclusive evaluation of the environmental sustainability of hydrophobic type V DES. A complete experimental eco-toxicological profile [82] is the necessary next step for a proper and thorough characterization of DES in terms of environmental sustainability and a comprehensive understanding of their impact on living systems and ecosystems.

CRediT authorship contribution statement

Sonia Martel-Martín: Writing – original draft, Visualization, Project administration, Investigation, Funding acquisition, Formal analysis, Data curation. **Maria Enrica Di Pietro:** Writing – original draft, Visualization, Project administration, Investigation, Funding acquisition, Formal analysis, Data curation. **Alberto Gutiérrez:** Writing – original draft, Visualization, Investigation, Formal analysis, Data curation. **Nuria Aguilar:** Writing – original draft, Visualization, Investigation, Formal analysis, Data curation. **Alfredo Bol-Arreba:** Writing – review & editing, Writing – original draft, Supervision, Resources, Methodology, Conceptualization. **Santiago Aparicio:** Writing – review & editing, Writing – original draft, Supervision, Resources, Project administration, Methodology, Funding acquisition, Conceptualization. **Fatima Matroodi:** Writing – original draft, Visualization, Investigation, Formal analysis, Data curation. **Barbara Rossi:** Writing – original draft, Visualization, Investigation, Formal analysis, Data curation. **Andrea Mele:** Writing – review & editing, Writing – original draft, Supervision, Resources, Project administration, Methodology, Funding acquisition, Conceptualization.

Declaration of competing interest

The authors declare that they have no known competing financial interests or personal relationships that could have appeared to influence the work reported in this paper.

Data availability

Data will be made available on request.

Acknowledgements

This work was funded by European Union (Horizon 2020 program, project WORLD: H2020-MSCA-RISE-2019-WORLD-GA-873005) and Agencia Estatal de Investigacion (Spain, PID2022-142405OB-I00). A portion of this work has been funded by European Union – Next Generation EU in the framework of the PRIN 2022 PNRR project POSEIDON - P2022J9C3R and PRIN 2022 project SEED4GREEN - Code 20223W4RT9. We acknowledge Elettra Sincrotrone Trieste for providing access to its synchrotron radiation facilities and for financial support under the SUI internal project (proposal number 20220430). We also acknowledge SCAYLE (Supercomputación Castilla y León, Spain) for providing supercomputing facilities. The statements made herein are solely the responsibility of the authors.

Appendix A. Supplementary data

Table S1 (specifications of chemicals used in this work); Table S2 (Force field parameterizations for MD simulations); Table S3 (specifications of systems used for MD simulations); Table S4 (systems for CG-MD simulations); Table S5 (protein docking results); Table S6 (diffusion coefficients); Table S7 (best-fit parameters for the Arrhenius model); Fig. S1 (molecular beading for CG-MD simulations); Fig. S2 (Solvation numbers from MD simulations); Fig. S3 (1D ^{1}H NMR spectra); Fig. S4 (self-diffusion coefficients from MD simulations). Supplementary data to this article can be found online at https://doi.org/10.1016/j.molliq.2024.126148.

References

[1] V. Hessel, N.N. Tran, M.R. Asrami, Q.D. Tran, N.V.D. Long, M. Escribá, J.O. Tejada, S. Linke, K. Sundmacher, Sustainability of green solvents – review and perspective, Green Chem. 24 (2022) 410–437.
[2] A. Prabhune, R. Dey, Green and sustainable solvents of the future: deep eutectic solvents, J. Mol. Liq. 379 (2023) 121676.
[3] D.O. Abranches, J.A.P. Coutinho, Everything you wanted to know about Deep Eutectic Solvents but were afraid to be told, Ann. Rev. Chem. Biochem. Eng. 14 (2023) 141–163.
[4] K. Shahbaz, F.S. Mjalli, G. Vakili-Nezhaad, I.M. AlNashef, A. Asadov, M.M. Farid, Thermogravimetric measurement of deep eutectic solvents vapor pressure, J. Mol. Liq. 222 (2016) 61–66.
[5] J. González-Rivera, C. Pelosi, E. Pulidori, C. Duce, M.R. Tiné, G. Ciancanceloni, L. Bernazzoni, Guidelines for a correct evaluation of Deep Eutectic Solvents thermal stability, Curr. Res. Green Sus. Chem. 5 (2022) 100333.
[6] L. Cichocki, D. Warminska, J. Luczak, A. Przyjazny, G. Boczkaj, New simple and robust method for determination of polarity of Deep Eutectic Solvents (DESs) by means of contact angle measurement, Molecules 27 (2022) 4198.
[7] A. Azzour, M. Hayyan, Are deep eutectic solvents biodegradable? Proc. Safety Environ. Prot. 176 (2023) 1021–1025.
[8] Q. Wen, J.X. Chen, Y.L. Tan, J. Wang, Z. Yang, Assesing the toxicity and biodegradability of Deep Eutectic Solvents, Chemosphere 132 (2015) 63–69.
[9] K.A. Omar, R. Sadequi, Physicochemical properties of deep eutectic solvents: a review, J. Mol. Liq. 360 (2022) 119524.
[10] B.B. Hansen, S. Spittle, B. Chen, D. Poe, Y. Zhang, J.M. Klein, A. Horton, L. Adhikari, T. Zelovich, B.W. Doherty, et al., Deep eutectic solvents: a review of fundamentals and applications, Chem. Rev. 121 (2021) 1232–1285.
[11] S.P. Ijardar, V. Singh, R.L. Gardas, Revisiting the physicochemical properties and applications of deep eutectic solvents, Molecules 27 (2022) 1368.
[12] L. Lomba, M.P. Ribate, E. Sangüesa, J. Concha, M.P. Garralaga, D. Errazquin, C. B. García, B. Giner, Deep eutectic solvents: are they safe? Appl. Sci. 11 (2021) 10061.
[13] G. Martínez-Martínez, G. Guillena-Townley, R.M. Martínez-Espinosa, Controversy on the toxic nature of deep eutectic solvents and their potential contribution to environmental pollution, Heliyon 8 (2022).

[14] Q. Zaib, M.J. Eckelman, Y. Yang, D. Kyung, Are deep eutectic solvents really green?: A life-cycle perspective, Green Chem. 24 (2022) 7924–7930.
[15] J. Afonso, A. Mezzetta, I.M. Marrucho, L. Guazzelli, History repeats itself again: Will the mistakes of the past for ILs be repeated for DESs? From being considered ionic liquids to becoming their alternative: the unbalanced turn of deep eutectic solvents, Green Chem. 25 (2023) 59–105.
[16] Y. Cao, S. Shan, J. Luo, Y. Li, R. Hao, Tuning toxic properties of polyethylene glycol-based deep eutectic solvents for achieving greener solvents, J. Mol. Liq. 369 (2023) 120879.
[17] I. Wazeer, M. Hayyan, M.K. Hadj-Kali, Deep eutectic solvents: designer fluids for chemical processes, J. Chem. Tech. Biotech. 93 (2018) 945–958.
[18] A. Mannu, M. Biangetti, S. Baldino, C. Prandi, Promising technological and industrial applications of Deep Eutectic systems, Materials 14 (2021) 2494.
[19] D.O. Abranches, J.A.P. Coutinho, Type V deep eutectic solvents: Design and applications, Curr. Opin. Green Sustain. Chem. 35 (2022) 100612.
[20] L. Zamora, C. Benito, A. Gutiérrez, R. Alcalde, N. Alomari, A. Al-Bodour, M. Atilhan, S. Aparicio, Nanostructuring and macroscopic behavior of type V deep eutectic solvents based on monoterpenoids, Phys. Chem. Chem. Phys. 24 (2022) 512–531.
[21] F.M. Fuad, M.N. Nadzir, A.H. Kamaruddin, Hydrophilic natural deep eutectic solvent: a review on physicochemical properties and extractability of bioactive compounds, J. Mol. Liq. 339 (2021) 116923.
[22] C. Florindo, L.C. Branco, I.M. Marrucho, Quest for green-solvent design: from hydrophilic to hydrophobic (Deep) eutectic solvents, ChemSusChem 12 (2019) 1549–1559.
[23] D.J.G.P. van Osch, C.H.J.T. Dietz, S.E.E. Warrag, M.C. Kroon, The curious case of hydrophobic deep eutectic solvents: a story on the discovery, design, and applications, ACS Sustainable Chem. Eng. 8 (2010) 10591–10612.
[24] M.H. Zainal-Abidin, M. Hayyan, W.F. Wang, Hydrophobic deep eutectic solvents: current progress and future directions, J. Ind. Eng. Chem. 97 (2021) 142–162.
[25] T. Hanada, M. Goto, Synergistic deep eutectic solvents for lithium extraction, ACS Sustainable Chem. Eng. 9 (2021) 2152–2160.
[26] N. Schaefer, M.A.R. Martins, C.N.N.S. Neves, S.P. Pinho, J.A.P. Coutinho, Sustainable hydrophobic terpene-based eutectic solvents for the extraction and separation of metals, Chem. Commun. 54 (2018) 8104–8107.
[27] Y. Liu, J.B. Friesen, J.B. McAlpine, D.C. Lankin, S.N. Chen, G.F. Pauli, Natural Deep Eutectic Solvents: properties, applications, and perspectives, J. Nat. Prod. 81 (2018) 679–690.
[28] D.J.G.P. van Osch, C.H.J.T. Dietz, J. van Sprosen, M.C. Kroon, F. Gallucci, M. van Sint, R. Tuinier, A search for natural hydrophobic deep eutectic solvents based on natural components, ACS Sustainable Chem. Eng. 7 (2019) 2933–2942.
[29] J.L. Trenzado, C. Benito, M. Atilhan, S. Aparicio, Hydrophobic Deep eutectic Solvents based on cineole and organic acids, J. Mol. Liq. 377 (2023) 121322.
[30] C. Florindo, L. Romero, I. Rintoul, L.C. Branco, I.M. Marrucho, From phase change materials to green solvents: hydrophobic low viscous fatty acid–based deep eutectic solvents, ACS Sustainable Chem. Eng. 6 (2018) 3888–3895.
[31] A.A. Elgharbawy, S.S.S. Putra, H.W. Khan, N.A.A.N. Azmi, M.S.A. Sani, N.A. Ilah, Hayyan, A.J. Jawaratnam, W.J. Basirun, Menthol and fatty acid-based hydrophobic deep eutectic solvents as media for enzyme activation, Processes 11 (2023) 547.
[32] A. Baena, A. Orjuela, S.K. Rakshit, J.H. Clark, Enzymatic hydrolysis of waste fats, oils and greases (FOGs): status, prospective, and process intensification alternatives, Chem. Eng. Proc. Int. 175 (2022) 108930.
[33] M. Devi, R. Moral, S. Thakuria, A. Mitra, S. Pauli, Hydrophobic Deep Eutectic Solvents as greener substitutes for conventional extraction media: examples and techniques, ACS Omega 8 (2023) 9702–9728.
[34] C. Florindo, N.V. Monteira, B.D. Ribeiro, L.C. Branco, I.M. Marrucho, Hydrophobic deep eutectic solvents for purification of water contaminated with Bisphenol-A, J. Mol. Liq. 297 (2020) 111841.
[35] A. Kyriakoudi, A. Tsiouras, I. Mourtzinos, Extraction of lycopene from tomato using hydrophobic natural deep eutectic solvents based on terpenes and fatty acids, Foods 11 (2022) 2645.
[36] S.B. Pour, A.R. Ebrahimzadeh, Structure and dynamics of hydrophobic deep eutectic solvents composed from terpene-fatty acids investigated by molecular dynamics simulation, J. Mol. Graph. Model. 114 (2022) 108180.
[37] N. Paul, T. Banerjee, Stability Mechanism of menthol and fatty acid based hydrophobic eutectic solvents: insights from nonbonded interactions, ACS Sustainable Chem. Eng. 11 (2023) 3539–3556.
[38] M. Busato, G. Mannucci, L.A. Rocchi, M.E. Di Pietro, A. Capocefalo, E. Zorzi, P. Csu, D. Veclami, F. Castiglione, A. Mele, A. Martinelli, P. Postorino, P. D'Angelo, The complex story behind a deep eutectic solvent formation as revealed by l-menthol mixtures with butylated hydroxytoluene derivatives, ACS Sustainable Chem. Eng. 11 (2023) 8988–8999.
[39] K. Kongpol, P. Chaihao, P. Shuapan, P. Kongduk, W. Chumglok, G. Yusakai, Therapeutic hydrophobic deep eutectic solvents of menthol and fatty acid for enhancing anti-inflammation effects of curcuminoids and curcumin on RAW264.7 murine macrophage cells, RSC Adv. 12 (2022) 17443–17453.
[40] C. Florindo, F.S. Oliveira, L.P.N. Rebelo, A.M. Fernandes, I.M. Marrucho, Insights into the synthesis and properties of deep eutectic solvents based on cholinium chloride and carboxylic acids, ACS Sustainable Chem. Eng. 2 (2014) 2416–2425.
[41] M. Hümmer, S. Kara, A. Liese, I. Huth, J. Schrader, S. Holtmann, Synthesis of (-)-menthol fatty acid esters in and from (-)-menthol and fatty acids – novel concept for lipase catalyzed esterification based on eutectic solvents, Mol. Cat. A 458 (2018) 67–72.
[42] A.R. Martins, E.A. Crespo, P.V.A. Pontes, L.P. Silva, M. Bülow, G.J. Maximo, E.A. C. Batista, C. Held, E.A.C. Pinho, E.A.C. Coutinho, ACS Sustainable Chem. Eng. 6 (2018) 8836–8846.
[43] K. Czamara, K. Majzner, M.Z. Pacia, K. Kochan, A. Kaczor, M. Baranska, Raman spectroscopy of lipids: a review, J. Raman Spectrosc. 46 (2015) 4–20.
[44] B. Rossi, C. Bottari, S. Catalini, A. Gessini, F. D'Amico, C. Masciovecchio, Synchrotron based UV Resonant Raman scattering for material science, in: V. P. Gupta, Y. Ozaki (Eds.), Molecular and Laser Spectroscopy, Elsevier, Amsterdam, The Netherlands, 2020, pp. 447–478.
[45] E.O. Stejskal, J.E. Tanner, Spin diffusion measurements: spin echoes in the presence of a time-dependent field gradient, J. Chem. Phys. 42 (1965) 288–292.
[46] S. Grimme, J. Antony, H. Krieg, A consistent and accurate ab initio parametrization of density functional dispersion correction (DFT-D) for the 94 elements H-Pu, J. Chem. Phys. 132 (2010) 154104.
[47] S.G. Balasubramani, G.P. Chen, S. Coriani, M. Diedenhofen, M.S. Frank, Y. J. Franzke, F. Furche, R. Grotjahn, M.E. Harding, C. Hättig, A.H.B. Helmich-Paris, et al., TURBOMOLE: modular program suite for ab initio quantum-chemical and condensed-matter simulations, J. Chem. Phys. 152 (2020) 184107.
[48] S. Simon, M. Duran, J. Dannenberg, How does basis set superposition error change the potential surfaces for hydrogen-bonded dimers? J. Chem. Phys. 105 (1996) 11024.
[49] R.F.W. Bader, Atoms in molecules, Acc. Chem. Res. 18 (1985) 9–15.
[50] L. Tian, F. Chen, Multiwfn: a multifunctional wavefunction analyzer, J. Comput. Chem. 33 (2012) 580–592.
[51] F. Fuster, B. Silvi, Does the topological approach characterize the hydrogen bond? Theor. Chem. Acc. 104 (2000) 13–21.
[52] E.R. Johnson, S. Keinan, P. Mori-Sanchez, J. Contreras-Garcia, A.J. Cohen, W. Yang, J. Am. Chem. Soc. 132 (2010) 6498–6506.
[53] BIOVIA COSMOtherm, Release 2021; Dassault Systèmes. http://www.3ds.com.
[54] A.P. Lyubartsev, A. Laaksonen, MDynaMix: a scalable portable parallel MD simulation package for arbitrary molecular mixtures, Comput. Phys. Commun. 128 (2000) 565–589.
[55] V. Zoete, M.A. Cuendet, A. Grosdidier, O. Michielin, SwissParam, a fast force field generation tool for small organic molecules, J. Comput. Chem. 32 (2011) 2359–2368.
[56] L. Martínez, R. Andrade, E.G. Birgin, J.M. Martínez, PACKMOL: a package for building initial configurations for molecular dynamics simulations, J. Comput. Chem. 30 (2009) 2157–2164.
[57] W.G. Hoover, Canonical dynamics: equilibrium phase-space distributions, Phys. Rev. A 31 (1985) 1695.
[58] M. Tuckerman, B.J. Berne, G.J. Martyna, Reversible multiple time scale molecular dynamics, J. Chem. Phys. 97 (1992) 1990–2001.
[59] U. Essmann, L. Perera, M.L. Berkowitz, T. Darden, H. Lee, L.G. Pedersen, A smooth particle mesh Ewald method, J. Chem. Phys. 103 (1995) 8577–8593.
[60] W. Humphrey, A. Dalke, K.V.M.D. Schulten, Visual molecular dynamics, J. Mol. Graph. 14 (1996) 33–38.
[61] M. Brehm, B. Kirchner, TRAVIS: a free analyzer and visualizer for Monte Carlo and molecular dynamics trajectories, J. Chem. Inf. Model. 51 (2011) 2007–2023.
[62] S. Halappanavar, S. van der Bruel, P. Nymark, L. Gaté, C. Seidel, S. Valentino, V. Zhernovkov, P.H. Danielsen, A. de Vizcaya, H. Wolff, T. Stoeger, A. Boyadziev, S.S. Poulsen, J.B. Sørli, U. Vogel, Adverse outcome pathways as a tool for the design of testing strategies to support the safety assessment of emerging advanced materials at the nanoscale, Part. Fibre Toxicol. 17 (2020) 16.
[63] S. Halappanavar, M. Sharma, H. Wallin, U. Vogel, K. Sullivan, A.J. Clippinger, Substance interaction with the lung resident cell membrane components leading to lung fibrosis. https://aopwiki.org/aops/173 (accessed May 1, 2024).
[64] S.J. Marrink, H.J. Risselada, S. Yefimov, D.P. Tieleman, A.H. de Vries, The MARTINI force field: coarse grained model for biomolecular simulations, J. Phys. Chem. B 111 (2007) 7812–7824.
[65] P. Vainikka, S. Thallmair, P.C.T. Souza, S.J. Marrink, Martini 3 coarse-grained model for type iii deep eutectic solvents: thermodynamic, structural, and extraction properties, ACS Sustainable Chem. Eng. 9 (2021) 17338–17350.
[66] O. Trott, A.J. Olson, AutoDock vina: improving the speed and accuracy of docking with a new scoring function, efficient optimization, and multithreading, J. Comput. Chem. 31 (2010) 455–461.
[67] G.D. Santos-Souza, A.M. Amado, A.M.R. Teixeira, P.T.C. Freire, G.D. Saraiva, G. S. Pinheiro, S.G.C. Moreira, F.F. de Sousa, C.E.S. Nogueira, Low-temperature phase transition of dodecanoic acid crystals: a study using Raman, powder X-ray diffraction, and density functional theory calculations, Cryst. Growth Des. 20 (2020) 281–290.
[68] E. Moreno, R. Cordobilla, T. Calvet, M.A. Cuevas-Diarte, G. Gbabode, P. Negrier, D. Mondieig, H.A.J. Oonk, Polymorphism of even saturated carboxylic acids from n-decanoic to n-eicosanoic acid, New J. Chem. 31 (2007) 947–957.
[69] M.E. Di Pietro, M. Tortora, C. Bottari, G.C. Dugoni, R.V. Pivato, B. Rossi, M. Paolantoni, A. Mele, In competition for water: hydrated choline chloride vs choline acetate deep eutectic solvents, ACS Sustainable Chem. Eng. 9 (2021) 12262–12273.
[70] G. de Araujo, M.E. Di Pietro, F. Castiglione, V. Vanoli, A. Mele, Insights into the effect of lithium doping on the deep eutectic solvent choline chloride: urea, Molecules 15 (2022) 7459.
[71] E. Posada, M.J. Roldán-Ruiz, R.J. Jiménez-Riobóo, M.C. Gutiérrez, M.L. Ferrer, F. Del Monte, Nanophase separation in aqueous dilutions of a ternary DES as revealed by Brillouin and NMR spectroscopy, J. Mol. Liq. 276 (2019) 196–203.
[72] N. Schaeffer, D.O. Abranches, L.P. Silva, M.A.R. Martins, P.J. Carvalho, O. Russina, A. Triolo, L. Oaccou, Y. Guinet, A. Hedoux, J.A.P. Coutinho, Non-ideality in thymol

+ menthol type V deep eutectic solvents, ACS Sustainable Chem. Eng. 9 (7) (2021) 2203–2211.
[73] G. de Araujo, M.E. Di Pietro, V. Vanoli, W. Panzeri, F. Briatico-Vangosa, F. Castiglione, A. Mele, Hydrophobic eutectogels: a new outfit for non-ionic eutectic solvents, Mater. Today Chem. 29 (2023) 101402.
[74] M.E. Di Pietro, F. Castiglione, A. Mele, Anions as dynamic probes for ionic liquid mixtures, J. Phys. Chem. B 14 (7) (2020) 2879–2891.
[75] U. Koch, P.L. Popelier, Characterization of C–H···O hydrogen bonds on the basis of the charge density, J. Phys. Chem. 99 (24) (1995) 9747–9754.
[76] J. Joseph, E.D. Jemmis, Red-, blue-, or no-shift in hydrogen bonds: a unified explanation, J. Am. Chem. Soc. 129 (15) (2007) 4620–4632.
[77] F. Bergua, M. Castro, J. Muñoz, C. Lafuente, M. Artal, L-menthol-based eutectic solvents: characterization and application in the removal of drugs from water, J. Mol. Liq. 352 (2022) 118754.
[78] G. Teixeira, D.O. Abranches, O. Ferreira, J.A.P. Coutinho, Estimating the melting temperatures of type V deep eutectic solvents, Ind. Eng. Chem. Res. 62 (31) (2023) 14638–14647.
[79] Y. Ma, L. Ma, X. Wang, High-pressure density of DL-menthol/octanoic acid eutectic solvents, J. Chem. Eng. Data 68 (3) (2023) 881–888.
[80] F. Chemat, H. Anjum, A. Shariff, P. Kumar, T. Murugesan, Thermal and physical properties of (Choline Chloride + Urea + L-Arginine) deep eutectic solvents, J. Mol. Liq. 218 (2016) 301–308.
[81] N.V. Veríssimo, F.A. Vicente, R.C. de Oliveira, B. Likozar, R.P.S. Oliveira, J.F. B. Pereira, Ionic liquids as protein stabilizers for biological and biomedical applications: a review, Biotechnol. Adv. 61 (2022) 108055.
[82] M. Vieira Sanches, R. Freitas, M. Oliva, A. Mero, L. De Marchi, A. Cuccaro, G. Fumagalli, A. Mezzetta, G. Colombo, M. Ferro, A. Mele, L. Guazzelli, C. Pretti, Are natural deep eutectic solvents always a sustainable option? A bioassay-based study, Environ. Sci. Pollut. Res. 30 (2023) 17268–17279.